THERMAL PROBE SCANNING OF LASER-POWDER BED FUSION ADDITIVE MANUFACTURING 316 STAINLESS STEEL

A Thesis Presented for the

Master of Science

Degree

The University of Tennessee, Knoxville

Chase Bernard Joslin

May 2026

ACKNOWLEDGEMENTS

Completing this milestone made me reflect on what had to happen in order to make this journey possible as well as the number of people who helped me along the way. Truly, I am humbled to be listed on this work given the help I received from everyone listed below. First, I thank The LORD for His grace and providential work in my life. Thank you to my incredible wife, Shawnee, for her faithful love and support. Thank you to my son, Brooks for being my motivation to complete this work. Thank you, Mom, for all of your sacrifices in life to allow me to succeed. Thank you, Dad, for giving me an inquisitive nature and a yearning to learn more. Thank you, Tiffanie and Bryce, for setting the success bar high for me. Thank you, Sean Yoder, for getting me introduced to the lab as an undergraduate. Thank you, Dr. Ryan Dehoff, for taking a chance on hiring me. Thank you, Dr. Michael Kirka, for giving me the freedom to grow in our group in PBF technologies. Thank you to my committee members Dr. Bradley Jared, Dr. Suresh Babu, Dr. Brett Compton, and Dr. Luke Scime for your encouragement and scrutiny in this work. Thank you also to Dr. Hsin Wang, Ryan Duncan, Dr. Vincent Paquit, Dr. Zack Snow, Clay Leach, Dr. Michael Sprayberry, Dr. Christine Cummings, Trevor McDonald, Julio Ortgea-Rojas, Andres Marquez-Rossy, Dr. Patxi Fernandez-Zelaia, Dennis Brown, Sarah Graham, Elizabeth Schmitt, Dr. Fred List, Keith Carver, and many others for your contributions to this work.

ABSTRACT

Laser-powder bed fusion (L-[hyphen]PBF) additive manufacturing (AM) continues to be a promising tool for fabricating complex geometries. However, both *in-situ* monitoring and *ex-situ* evaluation techniques cannot yet fully certify and qualify components due in part to the complex nature of melting dynamics at the build plane and laser interaction zone. This study began using a reflection configuration Flash Thermography (FT) to investigate the viability of detecting subsurface porosity *ex-situ*. From the FT results, active thermography was utilized to observe changes in thermal signatures on 316SS parts printed by L-PBF AM. By performing a low-power laser scan as a post-melt heat source, the surfaces of printed parts were thermally probed without remelting. A design of experiments (DOE) was performed to investigate parameters for the thermal probe scan (TPS). Imaging the TPS with a low frame rate near-infrared camera and an on-axis photodiode was found to identify near-surface pores *in-situ*. A dynamic multiscale convolutional neural network (DMSCNN) was trained to classify 2-dimensional (2D) visible-light, near-infrared, and photodiode images. A regression model was fit to predict percent porosity using anomaly class predictions from the DMSCNN as inputs. Data were segmented into 1mm x 1mm x 0.1mm zones. Parts printed with engineered pores had a regression correlation coefficient, R^2[squared], value of 0.795. While the regression model did not accurately predict percent porosity for control parts using anomaly class predictions. However, the TPS does show viability to detect large scale lack-of-fusion porosity in L-PBF *in-situ* process monitoring.

Keywords: Additive Manufacturing, Laser Powder Bed Fusion, Active thermography, Flash Thermography, Thermal Probe Scan, L-PBF, 316, Stainless Steel

TABLE OF CONTENTS

LIST OF TABLES

LIST OF FIGURES

CHAPTER ONE

INTRODUCTION AND GENERAL INFORMATION

Additive Manufacturing Introduction

Additive manufacturing (AM), colloquially called 3D printing, is a tried-and-true technology that offers design freedom that traditional manufacturing techniques, such as casting and forging, lack [1]. AM offers the ability to produce plastics, ceramics, and metals in a variety of technologies [2]. Each technology, such as photopolymerization of monomers to polymers, extrusion free forming of ceramics, or binder jetting of fine metal powder particles, is suited for a given material system [3]. One technology of particular interest to aerospace, medical, and energy applications is powder bed fusion (PBF). PBF uses a metal powder feedstock spread onto a flat bed, which is selectively melted, or fused, layer-by-layer based on a Computer Aided Design (CAD) or Stereolithography (STL) model [4]. These designed CAD or STL models can be complex, metal shapes such as lattices and heat exchangers. Each layer in a PBF print may be thought of as a "slice" of the desired part of a certain thickness, typically on the order of 50μm. As a result of chosen layer thicknesses, powder spreading technique, and fundamental technology, a subset of powder size distributions (PSD) in the range of 10μm - 150μm and machine build volumes ranging from a 3-inch cube to a 2-foot cube exist for a component designed for PBF AM.

One type of PBF, called Laser-PBF (L-PBF), uses a pulsed or continuous wave laser as a heat source to fuse a layer of spread powder particles within each slice. Because L-PBF operates using light quanta, or photons, to melt powder particles, there is

no charge build up on powder surfaces like that in electron-beam PBF (EB-PBF) [5]. Therefore, a finer PSD may be chosen to offer the advantage of printing small features. At its heart, L-PBF is a welding process. As such, this process takes place under an inert or near inert atmosphere. Typically using argon or nitrogen, this inert atmosphere prevents oxidation of printed parts at high temperatures. Furthermore, welding byproducts such as coarse spatter particles and fine condensate are generated during fusion which may affect the quality of printed material. Thus, ideally, a laminar flow of an inert gas is provided across the surface of the build plane to carry away particle ejecta from the weld.

During an L-PBF print, several factors contribute to the outcome of the part. On each layer, powder is spread across the previously melted layer, the laser selectively melts the slice in a scan strategy as determined by the operator, build pistons are moved down a distance equal to the layer thickness, all while laminar flow of inert gas cycles across the powder bed. During any layer, system anomalies may occur such as incomplete spreading of powder across the build surface, sudden blips in gas flow, and machine pistons jamming or moving an incorrect distance. In addition to system anomalies, print anomalies from laser welding may occur such as swelling of the print surface, delamination resulting from under-melting, and spatter ejecta from the meltpool landing on the powder and print surface. Both system and print anomalies occur during every L-PBF AM print, and prints may take thousands of layers and weeks of continuous printing. Which and what amount of system and print anomalies are acceptable is a question that spawned a branch of research termed *in-situ* process monitoring.

In-situ process monitoring mounts sensors onto an L-PBF machine to track progress, health, and build status throughout the printing process. Common sensors for L-PBF machines include visible-light cameras, thermal cameras in the near-infrared (IR) up to long-wave IR, on-axis and off-axis photodiodes, gas flow sensors, and acoustic sensors to alert the operator of both system and process anomalies. For a given process or system anomaly the operator may be able to take action to mitigate the error and resume printing as normal. For example, if incomplete powder spreading occurred on one layer, the operator may increase the powder dosing supply for future layers to prevent recurrence. In other cases, such as spatter ejecta landing on the powder bed and printed material, no amount of process design can account for inherent byproducts of laser welding and remove spatter from the print surface 100% of the time. This is a known phenomenon which is accepted as unavoidable. Thus, processing parameters are often chosen to reduce the likelihood of spatter particles causing as-printed flaws such as lack-of-fusion porosity. *In-situ* process monitoring can point operators to regions of interest which contain system and process anomalies which may result in flaws in the final part [6]. However, no matter the effectiveness of the *in-situ* process monitoring sensor package chosen for an L-PBF machine, other analyses are performed on parts *ex-situ* to determine the size, type, distribution, and location of flaws within as-printed parts.

Characterization Introduction

Ex-situ means of determining whether *in-situ* anomalies resulted in as-printed flaws may be categorized as a subset of non-destructive evaluation (NDE) and destructive evaluation (DE) techniques. NDE techniques useful to AM L-PBF parts include dye

penetrant, Eddy Current inspection, X-Ray Computed Tomography (XCT), and Thermography. NDE techniques useful to L-PBF AM parts include standard metallography, hardness testing, optical microscopy (OM), scanning electron microscopy (SEM), and transmission electron microscopy (TEM). *Ex-situ* techniques, broadly termed characterization, are generally considered ground truth as compared to *in-situ* process monitoring since both system and process effects take place for multiple layers influencing previously fused layers. What may have been a process anomaly on one layer may be healed on subsequent layers [7]. Furthermore, what may have been a process anomaly on one layer may indeed result in a flaw or even defect. To make the determination of which process anomalies constitute flaws or defects, further information must be garnered through *ex-situ* characterization.

An interesting branch of *ex-situ* characterization is thermography. Thermography is a technique used to track thermal energy emitted as radiative heat transfer using some imaging system. One such type of thermography called Flash Thermography (FT) which utilizes a near instantaneous, or Dirac pulse, pulse of energy. This pulse is typically in the form of broadband light, to thermally excite a surface and observe its temperature decay with time. This is performed using a camera which is sensitive to wavelengths in the 0.1 – 100 μm range, termed thermal radiation, caused by a thermal excitation [8]. Plotting temperature, or a proxy such as intensity, against time may reveal thermal build up which can be a result of factors ranging from surface effects to differences in thermal conductivity within composite materials.

In the case of carbon fiber reinforced polymers (CFRP) FT shows porosity, inclusions, and fiber damage due to differences in inherent thermal diffusivities of carbon and a surrounding polymer matrix [9]. In another example from Nagpure et. al, FT was used to show millimeter length scale defects within aged batteries by measuring differences in thermal diffusivity revealing cathode degradation with time and use [10]. Additionally, FT has been applied to metal powder bed surfaces for measuring weight-based densities down to 8% error [11].

In the case of metals, heat from FT is conducted away faster than composites such that typical camera sensors cannot capture sufficient frame rates to detect rapid changes in thermal emissions. FT data capture yields an exponential decaying curve of radiated photons, or intensity, plotted as a function of time in the milliseconds range. A local increase in thermal emissions often indicate the presence of a flaw, such as a pore, crack, or surface asperity all of which can have higher thermal emissions with time.

One intuitive difference from a process flaw as compared to nominal material is in total thermal emissions with time as illustrated in Figure 1.1. Although area under the curve may present differences compared to nominal material, relatively higher Volumetric Energy Density (VED) processing parameters also emit more heat with time. This can incorrectly present areas printed with relatively higher VED as process flaws. Raplee et. al showed that thermal decay rates may be a better predictor of process flaws that cause changes in thermal conditions locally [12]. However, perceived differences in thermally emissive data from metals may or may not be true indications of property differences due to emissivity. Emissivity is defined as the ratio of the radiation emitted

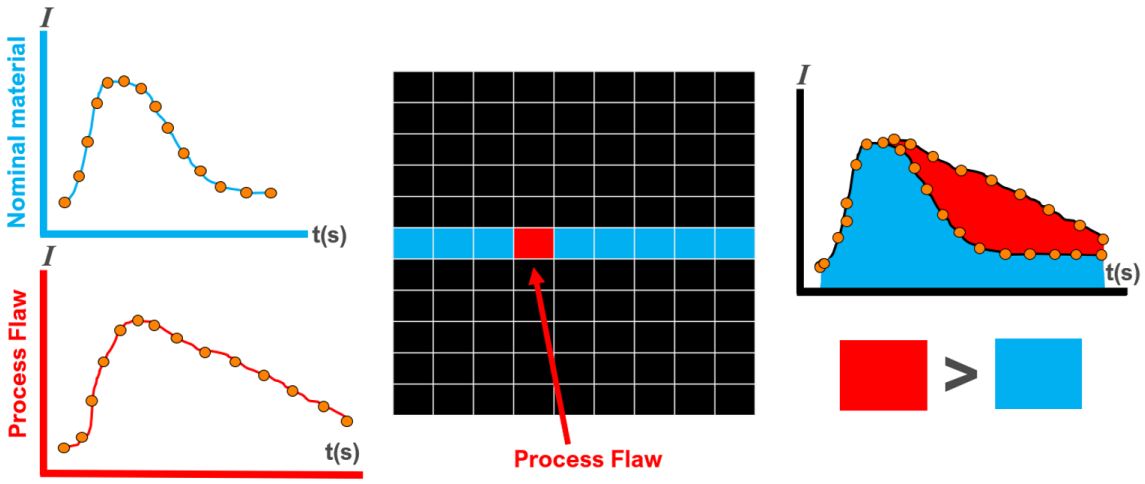

Figure 1.1. Intensity vs time decay plots of nominal material (left), a process flaw (middle), where the area under the curve is greater than that of nominally dense material (right).

by a material at a given temperature and wavelength to the radiation emitted by a blackbody at the same temperature for the same wavelength [8]. In short, emissivity is emitting efficiency. Emissivity is highly dependent on the surface qualities of the object being observed [13]. Surface effects from local changes in surface roughness and reflectivity may independently or codependently affect a material surface's emissivity. Hence emissivity is a complicating factor in any IR-camera setup, and its potential effects must be weighed prior to IR data analysis. Emissivity effects will be further discussed in Chapter Two: Literature Review and Chapter Four: *Ex-situ* Results section.

A process flaw may be defined in different ways but is here defined as an internal hole or a near-surface pore. When these process flaws are observed, the mechanism behind why it can be detected is a difference in thermal diffusivity. Due to a difference in thermal diffusivities of fully dense material vs porous material, the amount of radiation increases near the surface because of local heat build-up shown in Figure 1.2. An

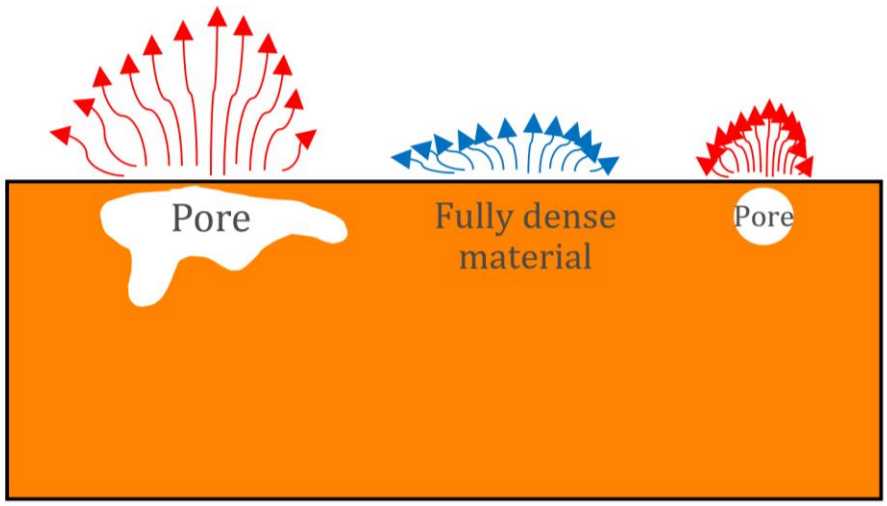

Figure 1.2. Surfaces positioned above pores will have relatively higher emissive powers than that of fully dense material due to a change in local heat transfer conditions.

internal pore acts as an insulating body through which heat cannot conduct. As a result, heat accumulates at a pore. That is, heat must propagate through a medium with a lower thermal diffusivity, or directionally "around" a pore. Using a thermal sensor, changes in thermal emissions may be observed. Radiation in the range of 0.1 μm – 100 μm are attributed to thermal effects shown in Figure 1.3. In an ideal setup, changes in temperature are governed by a one-dimensional heat transfer model derived by Maldague as:

$$T(0,t) = \frac{Q}{\sqrt{\pi \rho c k t}} e^{-\frac{d^2}{4\alpha t}} \tag{1}$$

where T is temperature in Kelvin, t is time in seconds, Q is energy flux in J/m², d is depth of an open face to the incident surface in meters, ρ is the material density in kg/m³, c is its specific heat capacity in J/(kg K), k is its thermal conductivity in W/(m K), and α is its thermal diffusivity in m²/s [14], [15]. While many of the material properties in Equation 1 change as a function of temperature, it is assumed herein that all properties are

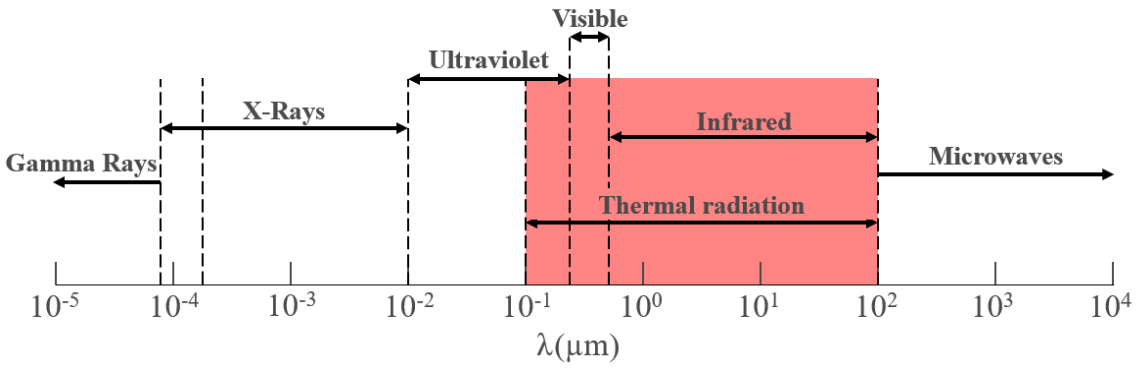

Figure 1.3. The light wavelength spectrum within which the 0.1 μm - 100 μm range are considered thermal radiation [8].

constant. Deviations from ideal setups and a 1D heat transfer model may be a result of many factors which will be discussed in Chapter Two: Literature Review and Chapter Four: *Ex-situ* Results sections.

A near-instantaneous pulse of energy is irradiated to the face of a sample and its ideal normalized decay curve for the heated mild steel sample can be observed in Figure 1.4. Heat transfers through the thickness of the sample and the opposite side heats up according to Equation 1. Thermal emissions on the back face are radiated and can be measured across the ultraviolet, visible, and IR spectrums shown in Figure 1.3. Metals dissipate heat relatively faster than materials such as ceramics and polymers. A decay curve comparing materials is shown in Figure 1.5, normalized by the highest temperature achieved for a constant energy input. In this case, it is normalized by the temperature achieved by polylactic acid (PLA). It is noted that because of the relative time that heat transfers through metal compared to other materials illustrated in Figure 1.5, challenges exist with capturing sufficiently high frames in FT for metals to observe differences in

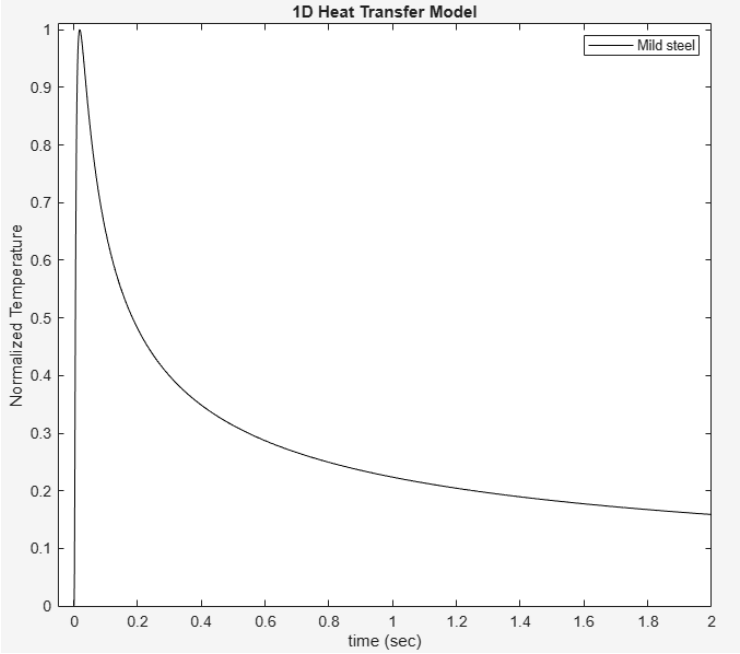

Figure 1.4. Normalized temperature response for one-dimensional heat transfer for mild steel heated by a Dirac pulse input.

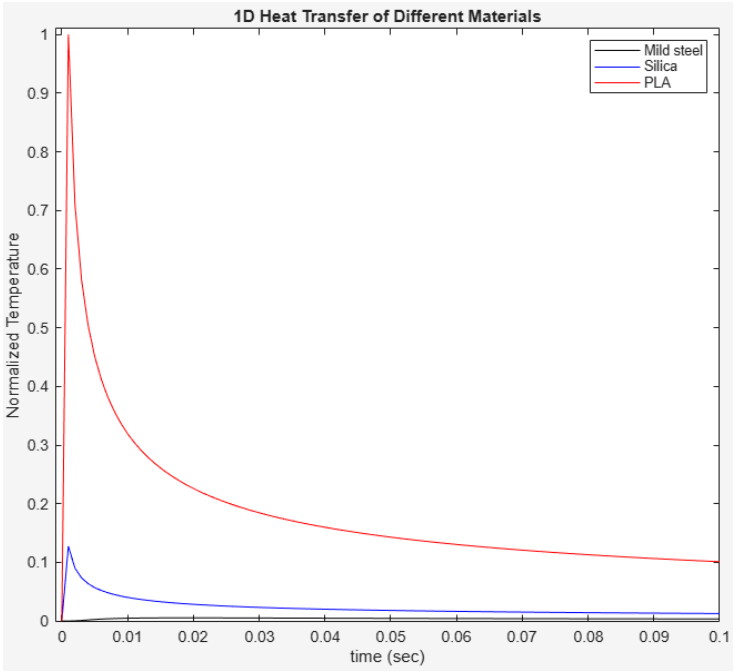

Figure 1.5. Temperature response for one-dimensional heat transfer for mild steel, silica, and PLA heated by a Dirac pulse input normalized by the maximum temperature achieved by all materials.

thermal transients during initial temperature decay. This is, in part, the reason there is less literature on FT applied to metals.

Regardless of setups with materials, assumptions must be made when performing analysis of FT data. First, we must assume that all heat is delivered instantaneously, called a Dirac pulse, at the start of the measurement. Thus, no heat is delivered through the decay time described by Equation 1. Second, heat is uniformly distributed across the part surface of interest. Third, we only observe heat transferred through the 1D part. Last, heat is only absorbed within an infinitesimally thin layer from a point heat source so that bulk heating does not occur into the part, allowing 2D heat transfer to be neglected.

Carslaw and Jaeger published the change in temperature for the reflection configuration which is listed here:

$$T(t) = \frac{Q\alpha}{kd}\left(1 + 2\sum_{n=1}^{\infty} e^{\frac{-n^2\pi^2 kt}{c_\rho d^2}}\right) \tag{2}$$

where all variables are the same from Equation 1 [16], [17]. Despite differences in configuration for measuring thermal response, the same trends shown in Figure 1.5 hold across different materials for one-dimensional heat transfer.

Given this introduction, the author proposed methods related to FT which could be applied inside an L-PBF printer. The committee recommended beginning with understanding what methods are applied *ex-situ* and to build off well-controlled and understood experiments before pursuing more complex *in-situ* process monitoring techniques. The following Literature Review took place to increase the author's knowledge and inform design for *in-situ* experiments.

CHAPTER TWO

LITERATURE REVIEW

All matter is continuously emitting electromagnetic radiation and absorbing electromagnetic irradiation [18]. Radiation emitted in the 0.1 – 100 μm range of the light spectrum shown in Figure 1.3 are of particular interest to thermographic techniques as this range of light is emitted as a result of thermal radiation. Observing thermal emissions from a surface is the heart of thermography. The particular branch of interest here, infrared thermography (IR-T), focuses on the IR band and excludes the ultraviolet and visible portions of the light spectrum. Here, any light incident upon a surface is considered irradiation whilst any light emitted is considered radiation.

IR-T is a tool used in myriad industries. Decades ago, IR-T was shown to reveal information about the internal structure of materials from variations in transient thermal surface emissions alone [19], [20], [21], [22]. There are diverse options for thermography which vary irradiation delivery, configuration modality, sensor type, and data analysis. Such examples include passive thermography (PT), active thermography (AT), and lock-in thermography (LI-T) [23], [24], [25], [26]. The method of interest in this study is to thermally excite materials and then to observe differences in resulting surface radiation, known as Flash Thermography (FT).

The crux of why IR-T NDE can reveal subsurface information about materials is because of differences in measured intensities during transient thermal events. When assumptions are made about constant thermal properties as a function of temperature, Equation 1 shows that temperature decay rates can only change if either the irradiative

heat, *Q*, or the thickness of a sample, *d*, changes. Thus, a material with a subsurface hole will respond differently to 1D heat transfer due to changes in *d* as compared to nominally dense material. However, if this hole is closed within a matrix, called a pore, we are introducing a new medium for heat transfer which must change thermal conductivity, density, and specific heat. Resultingly, surfaces above pores will cool more slowly and radiate more heat through time than nominally dense material as shown in Figure 1.2. Tracking heat radiated locally from the surfaces of materials is the focus of IR-T in this study and an attempt to learn information about internal structures of a material.

FT is based on the Parker Method for determining a material's thermal diffusivity [27]. Beginning with a flat disc of known thickness, heat is input instantaneously, and the maximum temperature is recorded. Parker et. al solved that the time required for the opposite side to reach half of the maximum temperature achieved on the irradiated side will measure thermal diffusivity α, measured in meters^2/second. Thermal diffusivity is determined according to Equation 2:

$$\alpha = \frac{1.38\, L^2}{\pi^2 t_{0.5}} \tag{2}$$

where L is the sample thickness measured in meters, and $t_{0.5}$ is the time for the radiating side of the disc to achieve half the maximum temperature of the irradiated side of the disc measured in seconds. Note that $t_{0.5}$ is not the square root of time, *t*. The elegance of the Parker Method is that no *a priori* knowledge of the material's thermal conductivity, density, specific heat, or even heat absorbed from the experiment is required to determine a material's thermal diffusivity. To this day, the Parker Method remains the ASTM standard for determining a material's thermal diffusivity [28].

The difference between the Parker Method and the FT setup used for this research is the configuration. The Parker Method utilizes a transmission mode in which the temperature of the opposite side of the disc is measured to obtain a bulk thermal diffusivity measurement. Here, a reflection mode is utilized such that the irradiated side is the same as the radiating side of the sample of interest [29]. It is noted that the term "reflection mode" is a naming convention used to describe the configuration and does not fully represent the physical mechanism of heat transfer at play. One advantage of the reflection configuration is that an arbitrarily thick sample can be used, and the transmission configuration also requires the ability to view both sides of a sample. Much research in the IR-T NDE community has originated from the Parker Method.

Shepard et. al showed that there are quantized limits to what can be observed from a thermographic signal due to camera sensor restraints [30]. Such limitations include frame rate and noise-equivalent temperature difference (NETD). NETD is how sensitive a camera is to changes in surface emissions with a change in temperature. When utilizing FT NDE with metals, these two parameters are of utmost importance for detecting subsurface pores since metals have a higher thermal conductivity and faster thermal decay time compared to ceramics and plastics, Figure 1.5.

There are many ways to analyze thermographic intensity signals with time. Simple methods include calculating the maximum temperature achieved, the area under the intensity curve, or the exponential thermal decay rate [12]. More exhaustive calculations include an averaging thermal decay rates in pulsed techniques, first- and second time-derivatives of intensity plots, or a time-over-threshold (TOT) which is the

time a pixel existed above a threshold temperature or intensity [12], [31], [32]. Further advanced techniques also exist such as dynamic thermal tomography and pulse phase thermography [33].

Regardless of the methods used to analyze data, it is necessary to distinguish background emissions from local intensities which may be indicative of subsurface pores. Thus, it is important to maximize signal-to-noise ratio (SNR). SNR is often used as a metric for a technique's efficacy. Heifetz et. al showed that increasing signal-to-noise ratios remains a barrier to detecting subsurface flaws in AM metals [34]. Their study suggested that ways to increase SNR in FT for metals include increasing the irradiation energy, selecting alloys with relatively lower thermal diffusivities, maximizing frame rates, performing denoising algorithms, or improving hardware limitations such as reducing NETD.

One obvious way to increase SNR in IR-T is to increase the size of the subsurface pore. Irrespective of material and IR-T technique, detectability of subsurface pores is directly related to their size and depth to surface [30], [32], [34], [35], [36], [37], [38]. A normalized predictor of flaw sizes is aspect ratio, or the ratio of the pore diameter to its distance from the surface. Aspect ratio is frequently explored as a metric for detectability in NDE using 1D heat transfer. There is consensus in literature that aspect ratios of greater than 9 in metals can be detected using *ex-situ* techniques [35]. Using modeling, Wallace et. al showed this can be pushed down to 6 [39]. Even lower aspect ratios have been reported using *in-situ* techniques [40].

One type of sample to explore varying aspect ratios is called a Flat-Bottomed Hole (FBH). FBH specimens are widely used in the NDE community for evaluating what aspect ratio of defects may be detected [41]. A FBH specimen is manufactured with known pores of varying aspect ratios and is particularly useful for calibrating FT setups to understand equipment and materials' limitations.

When observing a FBH specimen using FT, there is a critical assumption made about its flatness [27]. If the surfaces are not flat to a required tolerance, effects from emissivity can complicate any thermographic measurement data. Another issue affecting emissivity is the ratio of surface roughness to radiation wavelength. If the ratio of root-mean-square surface roughness, R_Q, to observed radiation wavelengths is less than 0.2, then surface roughness does not influence surface emissivity [13]. However, surfaces with values for this ratio above 1 directly impact emissivity values from captured IR-T data and result in measured temperatures that exceed the absolute temperature. The simplest way to avoid *ex-situ* emissivity effects from surface roughness and finish is to machine a surface flat and treat the surface with an optically black coating such as spray paint.

In attempts to account for emissivity in IR-T data related to L-PBF AM, studies have worked to measure absolute temperature *in-situ* accounting for differences between a powder bed and a melted surface [42], [43], [44]. Emissivity values have been measured for L-PBF materials in the range of 0.2 – 0.4 depending on material and temperature [45]. Kayacan et. al measured instantaneous temperatures within L-PBF systems [46] and noted that a confluence of complications arise when trying to calculate

absolute temperature values within an L-PBF system. That is, thermography depends on parameters which are not constant spatially or temporally. Factors such as surface roughness, texture, surface reflections, and view factor make a perceived surface temperature deviate from its true value. Nonetheless, representing thermal data is a worthwhile effort to correlate local differences in observed incoming photons as possible indications of differences in material properties. Thus, while it is extremely challenging to measure the absolute temperature, it is fortunately not necessary for the purpose of observing local variations in thermal diffusivity. Emissivity effects resulting specifically from surface roughness simply cannot be accounted for in a dynamic environment such as an L-PBF. Hence, *in-situ* analyses of IR-T, specifically Active Thermography (AT) in this thesis, will be presented without accounting for changes in emissivity.

AT is a type of IR-T which thermally and non-destructively excites a material surface whilst measuring its temporal response. AT and numerical models to predict porosity sizes and depths have been applied to plastics [47]. AT has been applied to L-PBF *in-situ* process monitoring. Typically, the laser itself is used as the excitation mechanism although this is not always the case. For example, Quercio et al. used Helmholtz coils to characterize iron losses of as-printed ferromagnetic steels as a function of build direction [48]. IR-T has also been applied *in-situ* using a coaxial thermal camera synchronized path infrared thermography (SPIT) to the laser to observe thermal radiation during melting [49]. The setup was useful for probing near the build plane a short time after melting. What is difficult in the case of the SPIT setup is spatter, soot, and other

meltpool ejecta obstructing the line of sight of the IR sensor which further complicates the accuracy of measurements.

The focus of the *in-situ* work in this study is most akin to work performed by Höfflin et. al, Breese et al, and Herzer et. al in which a secondary low-energy laser pass scans the surface of an L-PBF layer to induce local heating and observe variations in thermal signatures [50], [51], [52]. Because the detected intensities of both coaxial and off-axis sensors vary drastically due to dynamics within the plasma plume just above the build plane and molten meltpool, a special approach is required to see what is occurring at the build plane. The technique uses a low power laser pass to thermally excite the material surface without remelting. The key lies in avoiding remelting metal, which would generate further interactions that prohibit accurately measuring thermal decay of the solid surface. Notable distinctions from work by Höfflin, Breese, and Herzer in this thesis is to advance AT *in-situ* process monitoring by using specific sensors thermal emissions, the size and morphology of surrogate pores, the laser scan strategy, and the laser spot size. Specifics regarding these distinctions are covered in Chapter Three: *In-situ* Methods section.

Although AT may be a useful technique for *in-situ* NDE, it is important to acknowledge the state-of-the-art capabilities to target what can be sensed with different IR-T techniques. In the case of AT, regression models supported by machine learning (ML) can be used to predict porosity from thermal infrared image sequences [53]. The smallest reported feature detected in literature using thermography techniques on stainless steel components is 101 µm outer diameter at a depth of 127 µm using

unsupervised learning [54]. Given that typical laser cut powders range from 15 – 45 µm and common layer thicknesses are on the order of 50 µm, achieving resolutions and resolving powers down to this level will be a challenging task. Nevertheless, all *in-situ* process monitoring is a no-go test but not necessarily a go test. If a printed part cannot pass lower resolution inspection using *in-situ* process monitoring inspection, then it does not need to be inspected using *ex-situ* tools.

To summarize, the author hypothesizes that *in-situ* thermography data captured in an L-PBF AM printer using a low power laser pass after each layer has completed melting will create thermal signatures which can be uniquely observed by both on- and off-axis sensors. These sensors and their resulting image data will provide signatures that can be correlated to material properties that can be measured with *ex-situ* means. In our case, material density and how much porosity exists within printed L-PBF AM material is paramount. Although cited papers tend to use high frame rate IR cameras, this study utilizes a low frame rate near-IR (NIR) sensor and an on-axis photodiode.

CHAPTER THREE

MATERIALS AND METHODS

The remainder of this thesis will specify *ex-situ* or *in-situ* sections.

Ex-situ Materials

For the *ex-situ* experimental setup, flash thermography (FT) was initially conducted on multiple stainless steel (SS) samples, shown in Figure 3.1. The first idea was to make the sample as thin as possible for FT to minimize the amount of heat conduction through the sample and, as such, maximize the amount of time to detect residual heat. A 50 µm SS feeler gauge was laser drilled with different pulses to vary depth of holes, seven became thru-holes as shown in subfigure (a). Subfigure (b) shows a 316 SS coupon printed by L-PBF AM with thick and thin regions mounted in Bakelite using grinding metallography to achieve a flat face. This sample allowed the testing of what feature sizes can be detected. Subfigure (c) shows a 316 SS wavy thin wall support structure that was removed from an L-PBF print and tested to observe the influence of local surface roughness. Subfigure (d) shows a different 316 SS thin wall support structure from an L-PBF print mounted, ground, and polished using standard metallography and sand blasted to achieve a matte finish. This sample was chosen and prepared in this way to fix a flat and matte face for a thin metal sample after lessons learned from challenges encountered from other FT tests.

A FLIR mid-wave infrared (MWIR) 8501SC camera was fitted with a 50-mm lens and a 0.5” extender ring to improve resolution was used for FT. The camera was used in conjunction with a Hensel flash lamp and a Hensel Performing Light TRIA

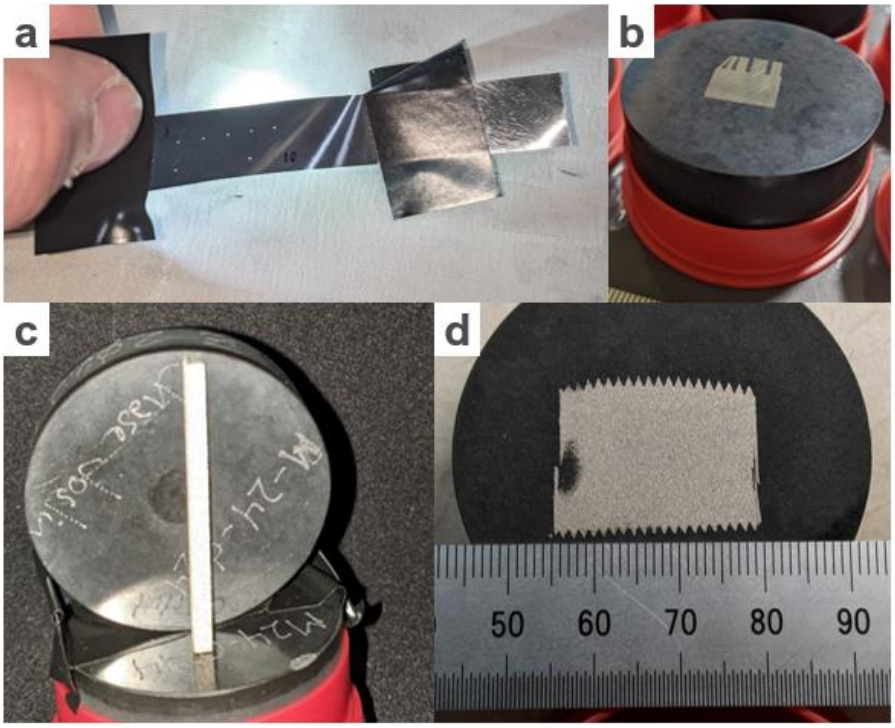

Figure 3.1. Stainless steel samples originally tested for FT including a 50 µm feeler gauge with laser-drilled thru holes (a), a mounted bulk and thin-walled sample (b), a thin wall support (c), and a mounted thin wall support (d).

6000S power source. The Hensel flash lamp had a Hensel EH Pro 6000 flash tube. The MWIR camera and flash lamp were placed side by side for reflection configuration FT.

Two flat bottom hole specimens were fabricated for this experiment, shown in Figure 3.2. An as-printed L-PBF 316 stainless steel (SS) FBH specimen is termed FBH1, and the machined A36 steel FBH specimen is termed FBH2. Base dimensions of each FBH specimen are 50.8 mm x 50.8 mm x 6.35 mm as shown in Figure 3.3. An array of 20 holes was printed into the FBH1 specimen with varying diameter and bottom wall thickness, defined as the distance from the hole bottom to the back surface. FBH1 contains five columns with diameters of 0.5, 1.0, 3.0, 5.0 and 10 mm. The four rows use varying bottom wall thickness of 0.75, 1.0, 3.0 and 5.0 mm.

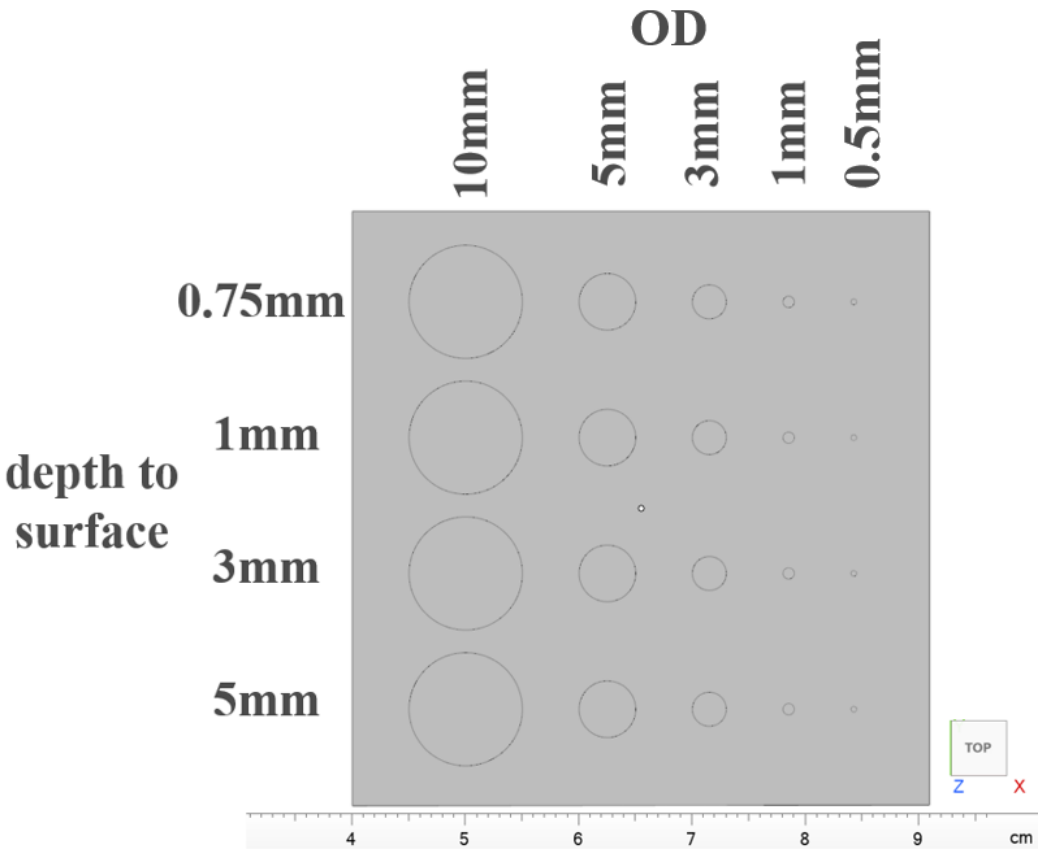

Figure 3.2. A top-down view of the FBH1 specimen outlining varying ODs and depths to surface.

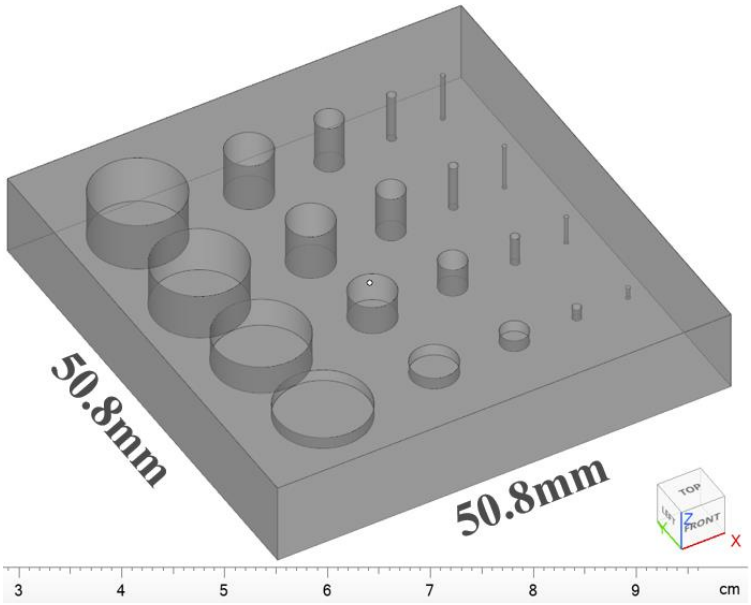

Figure 3.3. A transparent view of the FBH1 specimen as designed for printing with holes facing up.

FBH1 was printed with 3 mm of base stock for electrical discharge machining (EDM) to the desired thickness. FBH1 was printed from a SS 316 powder feedstock from Praxair with a chemical certification shown in Table 3.1 The PSD was 15 – 45 µm.

A Colibrium Concept Laser M2 Cusing with a 400W continuous wave fiber laser used to print the FBH1 specimen was used to print the *in-situ* samples. The FBH2 specimen was machined with a Haas TM-1 using a flat endmill. The 1 mm and 0.5 mm OD holes were easily able to be printed given the print orientation and resolution of the laser printer, but a machined A36 steel specimen did not have the same size holes machined due to system dynamics challenges associated with milling high aspect ratio holes without puncturing through the opposite side of the sample.

FBH2 was machined with the same rows of hole depths, but only the 3, 5, and 10mm hole diameters. Since machining high aspect ratio holes is difficult, the columns of 0.5 and 1.0mm diameter holes were omitted in the sample. FBH2 was machined from 0.25" thick A36 steel stock. The as-printed and as-machined FBH samples are shown in Figure 3.4**Error! Reference source not found.**. To reduce emissivity effects on the surface, each sample was painted with KRYLON flat black spray paint, Figure 3.5.

A flash box was initially created using a cardboard box lined with black neoprene acting as an IR flock, Figure 3.6 An improved version of the flash box was constructed using aluminum and balsa wood lined with black neoprene, Figure 3.7. The improved FT design made for more repeatable setups, further reduced ambient light, and was made larger for the flash lamp and MWIR camera to be placed at the opening without obstructing the camera's view.

Table 3.1. Manufacturer's chemical certification of AM powder feedstock for FBH1.

Element	Weight %
C	< 0.005
Co	0.08
Cr	17.01
Cu	0.00
Fe	Bal
Mn	1.29
Mo	2.48
N	0.01
Ni	12.67
O	0.03
P	< 0.005
S	0.005
Si	0.59
Total other	< 0.1

Figure 3.4. As-printed FBH1 sample (left) and as-machined FBH2 sample (right).

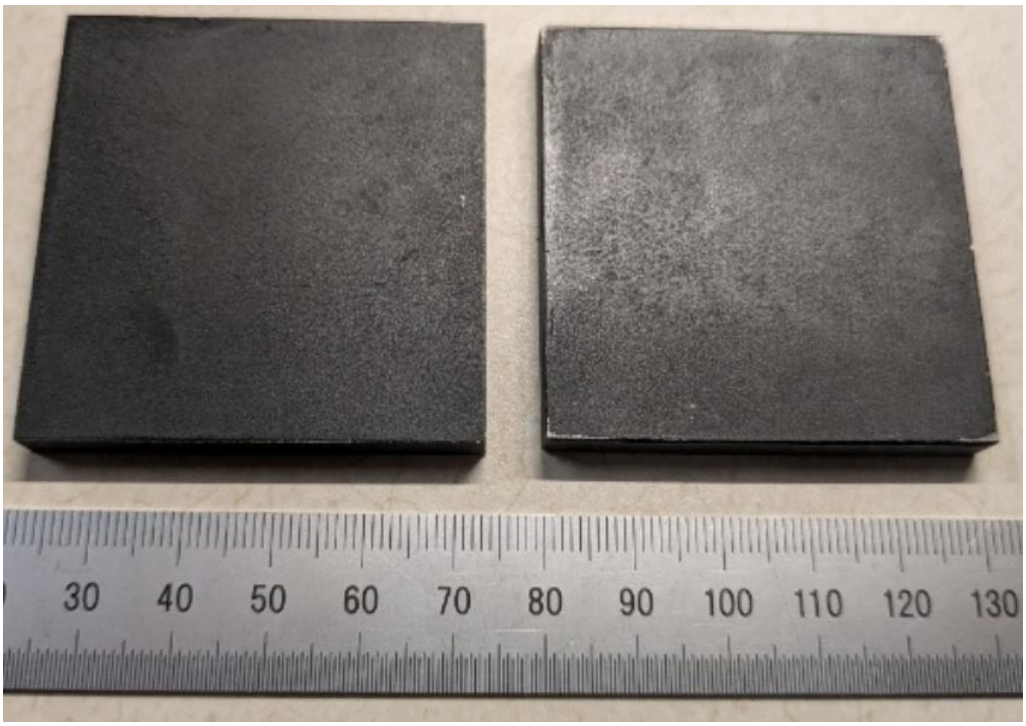

Figure 3.5. Black spray-painted solid face of the FBH1 sample (left) and the FBH2 sample (right).

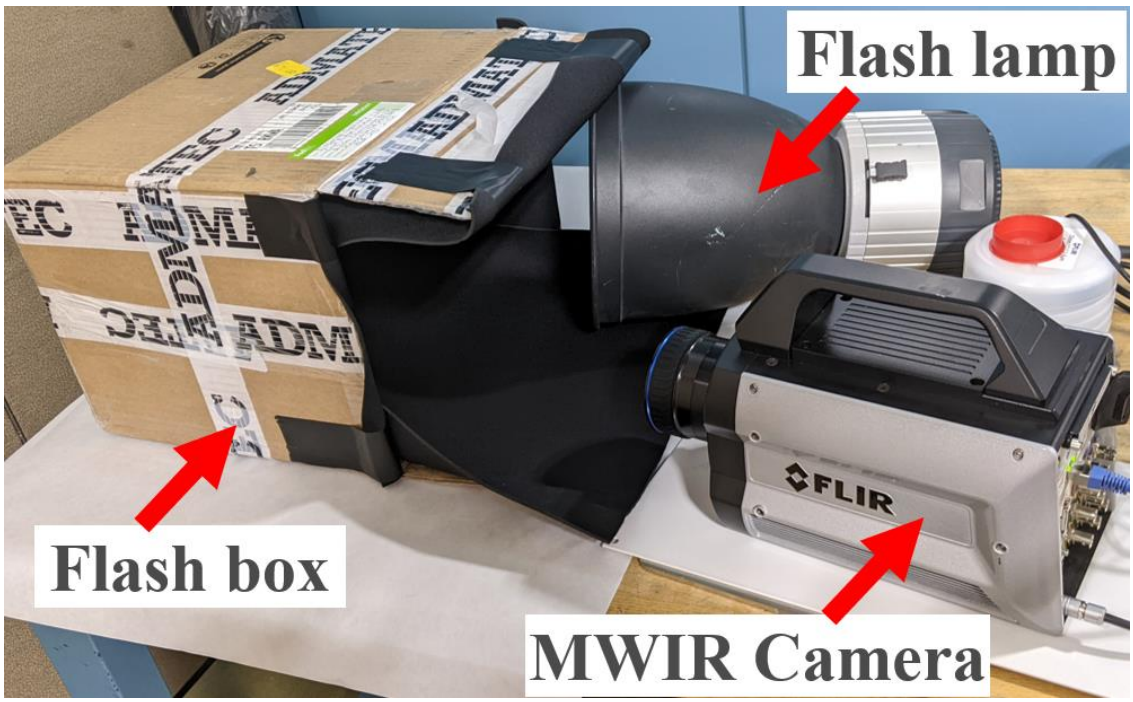

Figure 3.6. Initial flash box setup to image a sample using the flashlamp and MWIR camera.

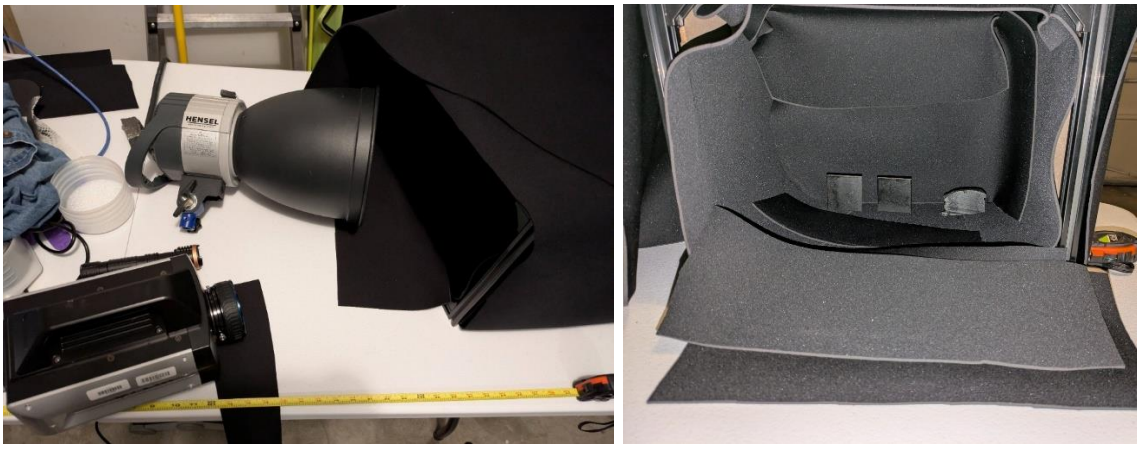

Figure 3.7. Improved flash box setup to image a sample using the flashlamp and MWIR camera (left) and the inside of the box with test samples during a flash pulse (right).

Ex-situ Methods

For the *ex-situ* experiment, a FLIR mid-wave infrared (MWIR) 8501SC high-frame rate camera capable of up to 2 kHz frame rate was selected. The high speed MWIR camera was selected both for its high frame rate to capture rapid heat dissipation from testing metal samples and for its configurability during test setups with different lenses and extender ring hardware. The camera was fitted with a 50-mm lens and a 0.5" extender ring to improve resolution. The camera's working distance, proper alignment, height, and focus were tested for the reflection configuration FT setup. The camera was used in conjunction with a Hensel flash lamp and a Hensel Performing Light TRIA 6000S flash lamp. The Hensel flash lamp was used with a Hensel EH Pro 6000 flash tube capable of producing near-instantaneous diffuse 6 kilo-Watt broadband light pulses. Pulse energies for the flash lamp were varied from 3 – 6 kW and measured to be less than 7 ms. The order of operations was to manually begin recording the IR video and trigger the flash pulse shortly thereafter. Each video was captured for approximately 5 seconds.

In-situ Materials

316 stainless steel powder was used for the *in-situ* experiments using the same chemical certification shown in Table 3.1.

The M2 was fitted with three sensors critical to the analysis of this *in-situ* study. The first of which is a Basler acA5472-17um 20 MP grayscale visible-light (VL) camera fitted with a MidOpt BP500 filter sensitive across the VL spectrum shown in Figure 1.3. This VL camera is used to capture three images per layer. Two are captured after all laser scanning has concluded, one with a side and one with a top-down lighting, termed post-fusion images. The third image is captured after the subsequent powder layer has been applied termed, post-spreading. The second sensor is the same model Basler acA5472-17um 20 MP grayscale sensor, configured as a thermal emissions camera (TEC) fitted with MidOpt ND090 and BN850 filters sensitive in the 790 – 820 nanometer (nm) range. The TEC is used for low-frame rate of 2 – 5 frames per second capture of thermal emissions of all melting during a given layer. The third is an on-axis ThorLabs PDA100A2 on-axis photodiode with a NF1064-44 laser cutoff filter. The photodiode is sensitive in the 320 – 1100 nm range and captures emissions at a rate of approximately 40kHz. One drawback to using on-axis sensors is that views can be obstructed by the plasma plume at the build plane during powder melting.

A total of seven images were captured each layer. This includes three visible-light images, Figure 3.8, two NIR images, Figure 3.9, and two photodiode images, Figure 3.10. The VL images in Figure 3.8 are captured with varying lighting conditions and timing. Namely after the layer has completed melting, or post-fusion, with two lighting conditions, a side and top-down lighting. The third VL image is after the subsequent

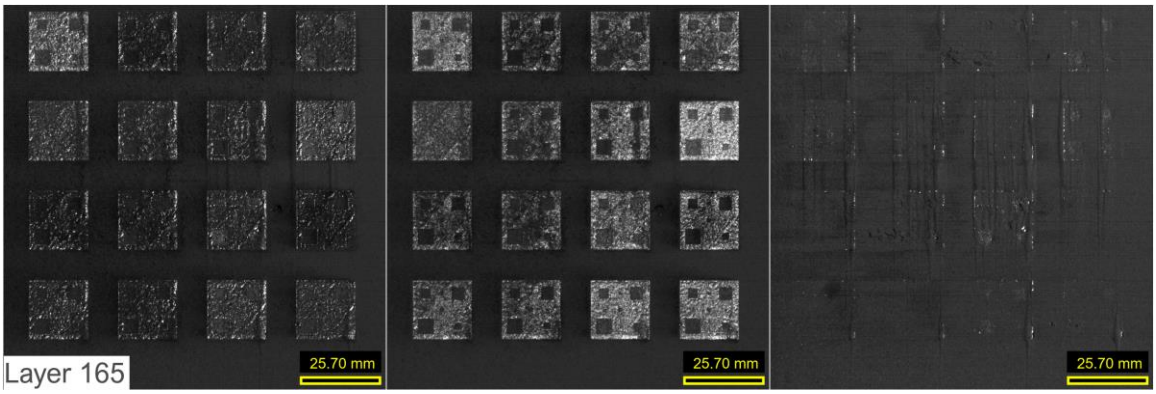

Figure 3.8. VL images captured each layer. Post-fusion with side-lighting (left), post-fusion top-down lighting (middle), post-spreading side-lighting (right).

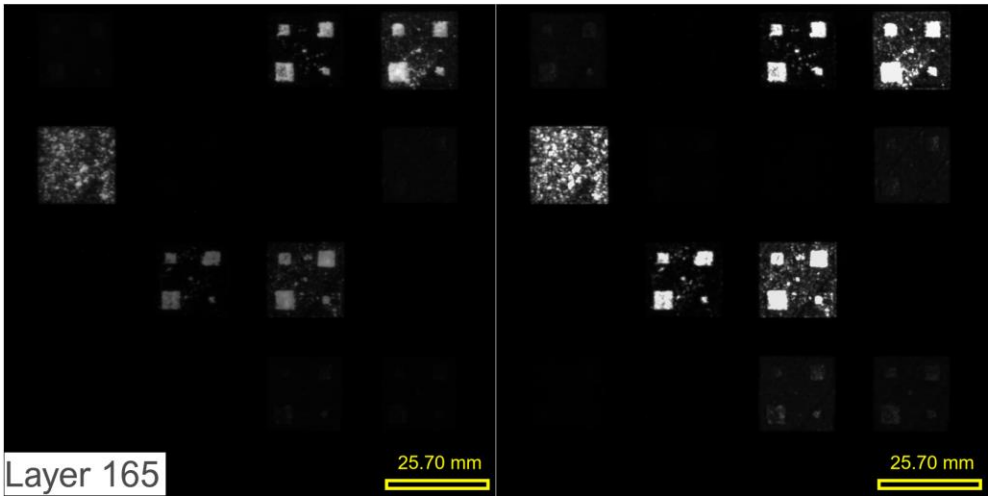

Figure 3.9. NIR images captured each layer for only TPS. Time-integrated image (left) and max (right).

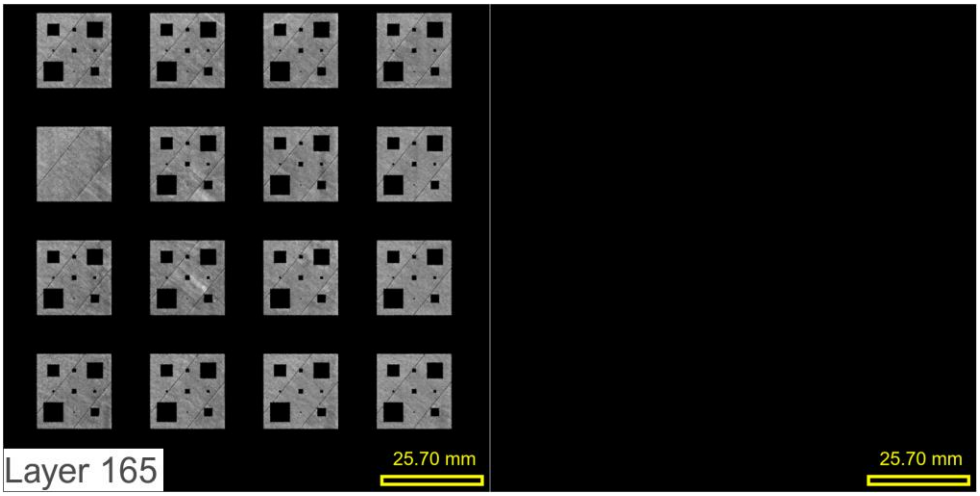

Figure 3.10. Two photodiode images captured each layer. Intensities from the melt (left), and TPS (right).

powder layer has been applied, or post-spreading, with side-lighting. Figure 3.9 shows the two thermal images captured exclusively during the thermal probe scan (TPS) described in the next section, Chapter Three: *In-situ* Methods. Two photodiode images are captured shown in Figure 3.10, one during the melt and the other during the TPS. It is critical for the purpose of this study to understand that the NIR images are captured for only the TPS. As will be described later and may be noted from Figure 3.10 immediately, the photodiode only captured intensities during the melt and not during the TPS. For the remainder of this study, all NIR images are exclusive to the TPS, and all photodiode images are related to only the melt.

In-situ Methods

A Concept Laser M2 Cusing was used for one *in-situ* experiment termed the TPS DOE. Cubes with engineered rectangular-prism voids were designed as shown in Figure 3.11. On a layer with engineered porosity, there were nine squares of varying sizes shown in Figure 3.12. All cubes were printed using nominal parameters for 316 SS, Power of 370 W, laser speed of 1350 mm/s, hatch spacing of 90 µm, layer thickness of 50 µm, and a laser spot size of 130 µm. The engineered porosity varied thickness at 2 layers, 6 layers, and 10 layers by height within the cube as shown in a front-view in Figure 3.13. 16 total cubes were designed in the print with identical geometries. An arbitrary layer that includes engineered porosity is shown in Figure 3.14. Note that there is a control block designed into this study, namely part 9 which does not include engineered porosity and is a solid block. A different type of control block related to the TPS will be discussed shortly.

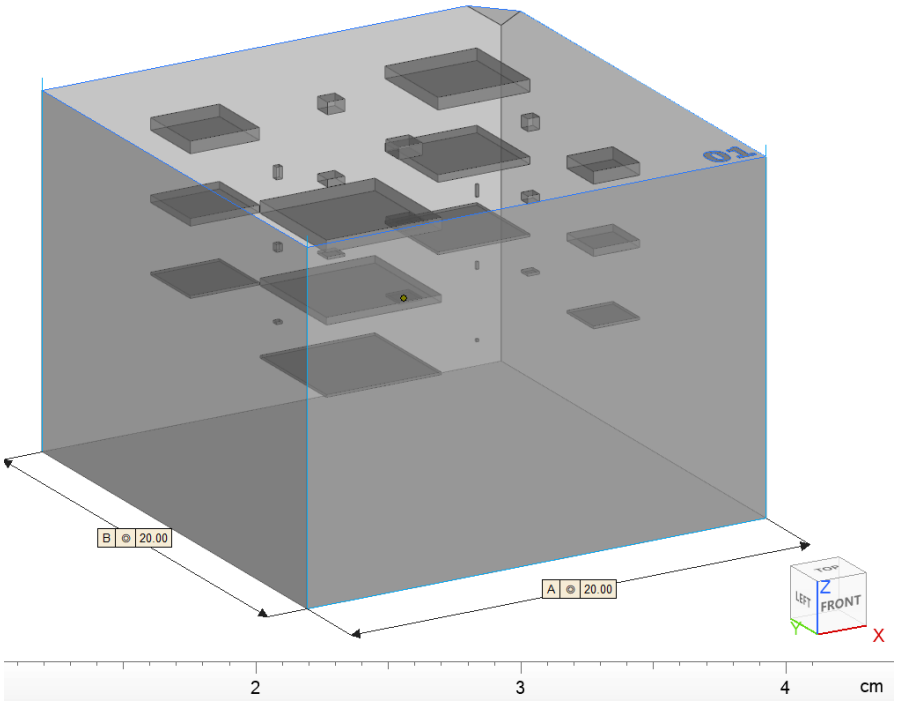

Figure 3.11. Each cube was designed with the same engineered porosity.

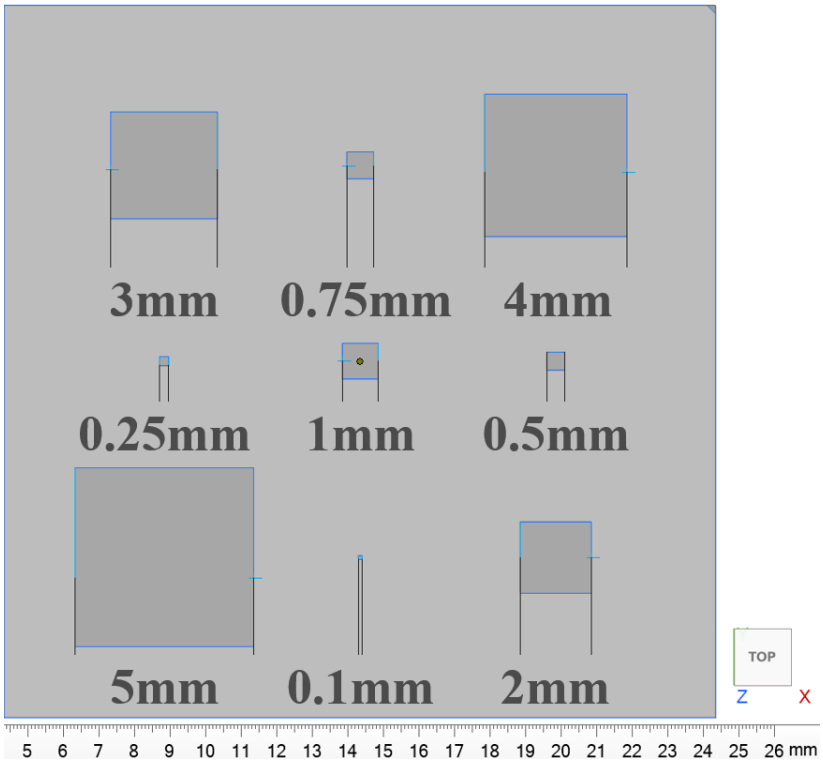

Figure 3.12. A top-down view of each cube with engineered porosity listing designed side length.

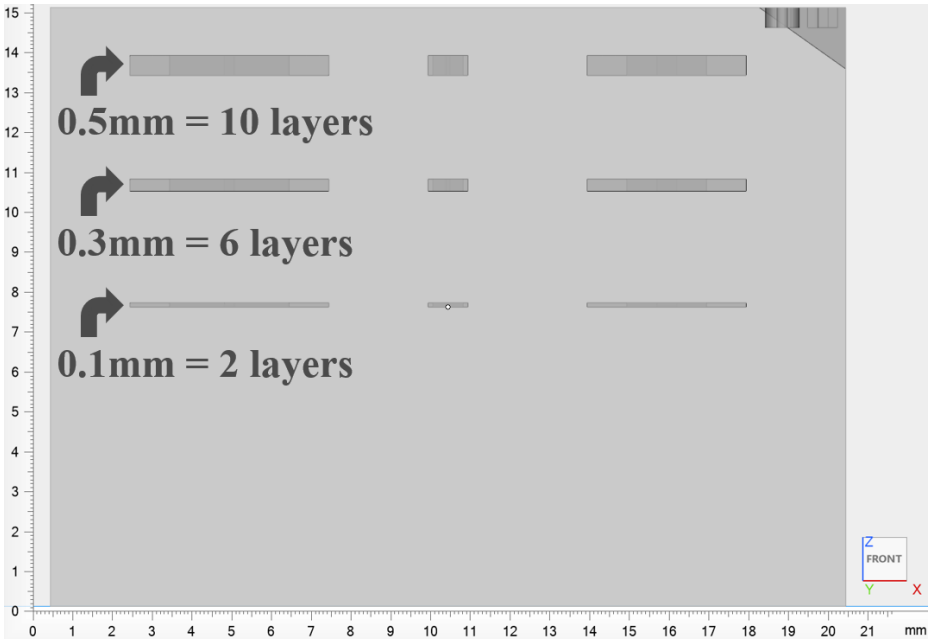

Figure 3.13. Front view of the sets of engineered porosity varying thickness according to Z-height.

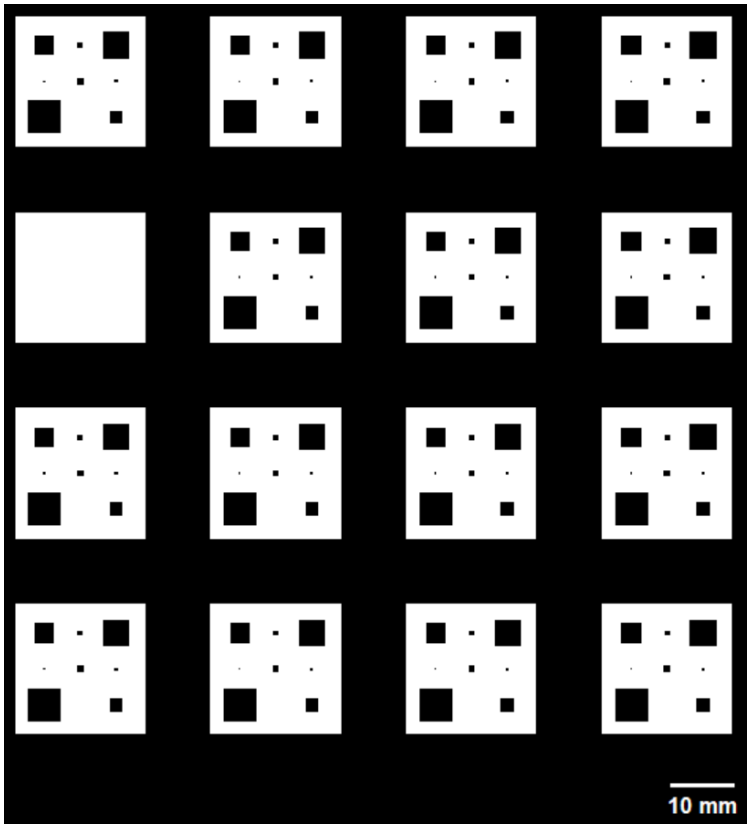

Figure 3.14. A top-down view of a layer including engineered pores. The control block, part 9, is solid.

The uniqueness of the process explored in this stage of the research is the introduction of a thermal probe scan (TPS). It is a low power secondary laser pass, represented in Figure 3.15. On a layer, all cubes are melted normally then the TPS is applied to all cubes except the control block part 9. The intent is to thermally excite the solidified metal surface without remelting to then observe the resulting radiation. The hypothesis is that local higher emitted intensities will correspond to the location of subsurface porosity due to lack of thermal conduction paths, similar to patterns revealed by the FT *ex-situ* experiments. To eliminate scan path heating from shorter vector lengths [55], a simple raster pattern is performed in which the laser direction does not rotate per layer. This scan strategy ensures that vector length is constant across the part.

Table 3.2 lists values for the standard melt which were constant across all cubes and, to test a range of parameters that may change local heat input from the TPS. To explore and optimize the TPS parameters, laser power, hatch spacing, laser spot size, and the number of passes were all varied using the values in Table 3.2. As shown in Figure 3.16, a single TPS was used for Parts 1-7 and a double TPS was used for Parts 9-16. In the double TPS pass, the second scan was rotated 90° from the first but fixed for each layer. Constant parameters were velocity at 1000 mm/s and layer thickness at 50 µm.

A single value metric often used for comparing processing parameters is Volumetric Energy Density (VED) measured in J/mm³, which is defined as:

$$\mathrm{VED} = \frac{\mathrm{P}}{v\,h\,t} \tag{3}$$

where P is laser power measured in W, v is laser velocity measured in mm/s, h is laser hatch spacing measured in mm, and t is layer thickness measured in mm.

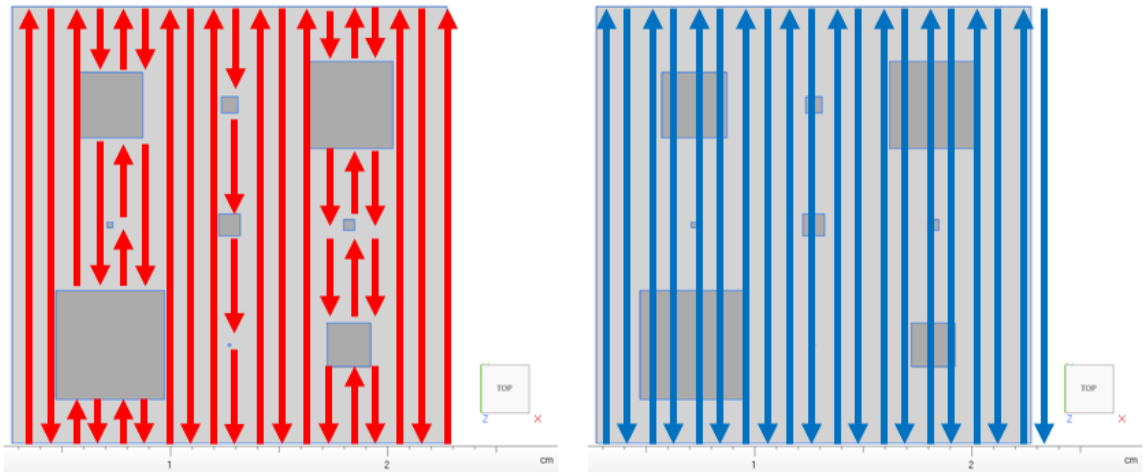

Figure 3.15. A top-down view of the lasing order for each layer containing engineered porosity in which melting occurs first (left) and the TPS occurs second (right). The TPS scans across the entire part bounding box irrespective of that layer's printed geometry.

Table 3.2. Processing parameters explored in the TPS study. Bold text refer to the two control blocks which excluded a TPS for part 8 or engineered pores for part 9.

Part ID	Power (W)	Hatch (mm)	Spot Size (mm)	Number of Passes	VED (J/mm³)
1	10	0.025	0.050	Single	8
2	10	0.050	0.050	Single	4
3	25	0.025	0.050	Single	20
4	25	0.050	0.050	Single	10
5	10	0.025	0.500	Single	8
6	25	0.025	0.500	Single	20
7	50	0.025	0.500	Single	40
8	-	-	-	**TPS Control**	-
9	**50**	**0.025**	**0.500**	**Double**	**40**
10	10	0.025	0.050	Double	8
11	10	0.050	0.050	Double	4
12	25	0.025	0.050	Double	20
13	25	0.050	0.050	Double	10
14	10	0.025	0.500	Double	8
15	25	0.025	0.500	Double	20
16	50	0.025	0.500	Double	40

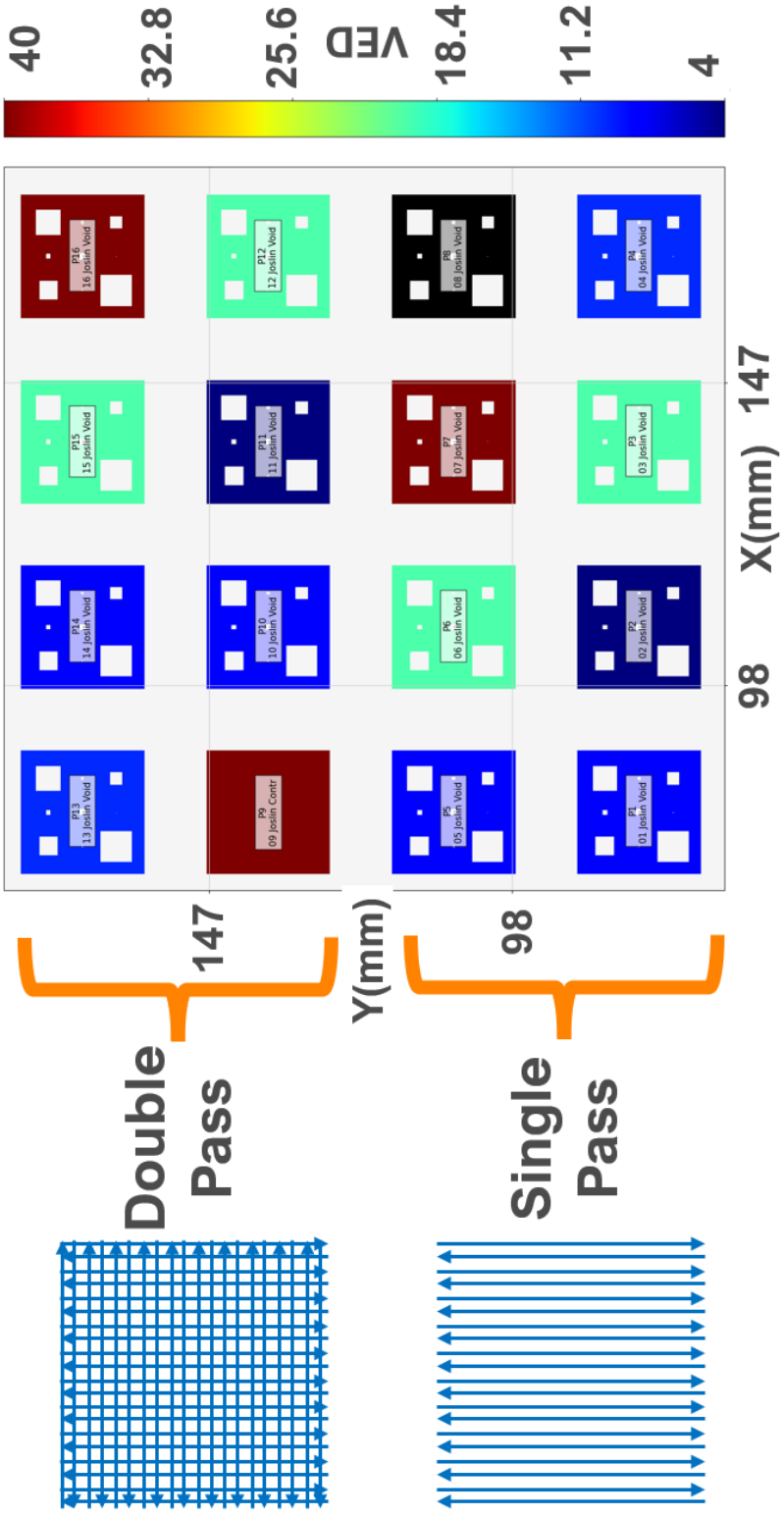

Figure 3.16. The number of passes and scan strategy applied to each set of cubes.

It is critical to eliminate effects from scan strategy as much as possible while performing the TPS so as to avoid heating effects resulting from coalescing meltpools with shorter vector lengths [53]. Local heat build-up from scan strategy may result in undesired remelting of the part surface. The scan strategy chosen to avoid this issue was a simple raster pattern in which the hatching did not rotate per layer. This scan strategy ensures that line length is constant across the part and would not vary across layers.

Two control parts were included in this study. Note that the two control blocks Parts 08 and 09 are in bold text. Part 08 has no TPS and part 09 does not have engineered pores. To test whether thermal signatures could be observed without using TPS, Part 8 was printed with pores but no TPS. Since its top surface was melted last during each layer's print sequence, part 8 would be warmer than the other cubes at the time of camera triggering to capture thermal emissions by the TEC. Therefore, it would be the most advantageous scenario that PT would be sufficient to capture thermal signatures indicating the presence of subsurface pores. A second control part, part 9, did include TPS but its part geometry was solid without the engineered pores. Here it is possible that the TPS could indicate the presence of subsurface pores without generating them artificially in the CAD model. Analysis on these cubes in particular are most interesting to understand the necessity and utility of the TPS.

During the TPS design-of-experiments (DOE), images captured as described in the *In-situ* Materials section are shown in Figure 3.8, Figure 3.9, and Figure 3.10. After the TPS DOE was completed, the captured *in-situ* data was gathered and put into Oak Ridge National Laboratory's (ORNL) Manufacturing Demonstration Facility's (MDF)

Peregrine software [56], [57]. Peregrine is a suite of tools designed for PBF *in-situ* data collection and analysis. From Peregrine, all *in-situ* images are captured each layer and may be viewed using both a spatial (XYZ location) and temporal (layerwise) basis. The imaging and other *in-situ* data are then encoded into a feature vector illustrated in Figure 3.17**Error! Reference source not found.**. In this form, powder bed images were annotated to train a Dynamic Multi-label Convolutional Neural Network (DMSCNN) to rapidly characterize anomaly classes within PBF images [56]. Anomaly classes are anything that an experienced operator can name to understand and describe a layer of a printed part. While not anomalous, the two base classes included in any PBF analysis are Powder and Printed.

Building off work from Scime et. al, Figure 3.18Figure 3.18 shows anomaly classes defined for the purpose of the TPS DOE [58]. Where this study varies from previous work is in the timing of data capture for the thermal images as well as segmented capture times and image conversion for the photodiode data. Recall that, specifically for the TEC, no thermal emissions were captured during the standard melt of all parts. It was only after melting had completed that TPS began and the TEC captured data for only the TPS of all parts. However, the on-axis photodiode data was captured and then separated temporally post-build for both the melt and for the TPS. As will be shown in Chapter Four: *In-situ* Results, the photodiode data for the TPS was nearly zero.

The DMSCNN was trained by the author and was performed using objective tools and knowledge. For example, printed material only exists where the CAD model was

designed on a layerwise basis. Most classes were selected in training based on simple threshold tools above or below a particular grayscale value from 0 – 255. Two new

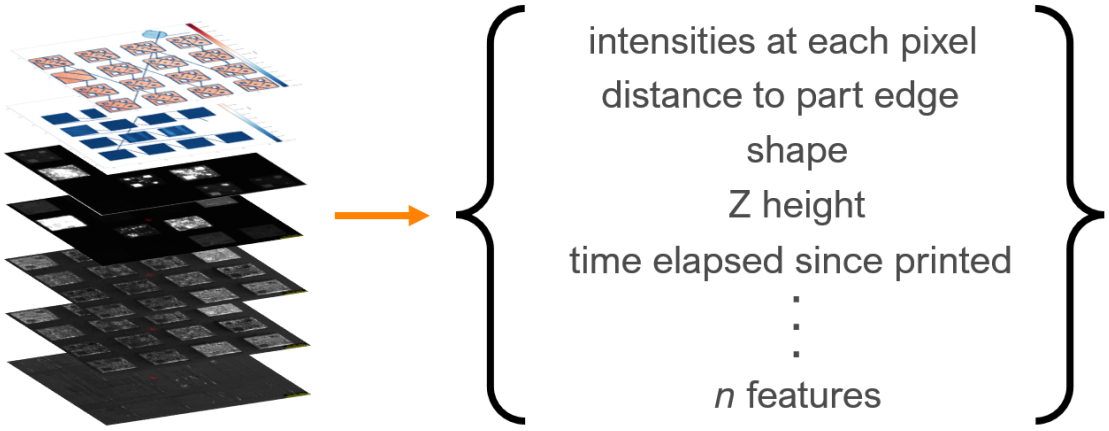

Figure 3.17. An illustration of example features encoded within the feature vector for every pixel.

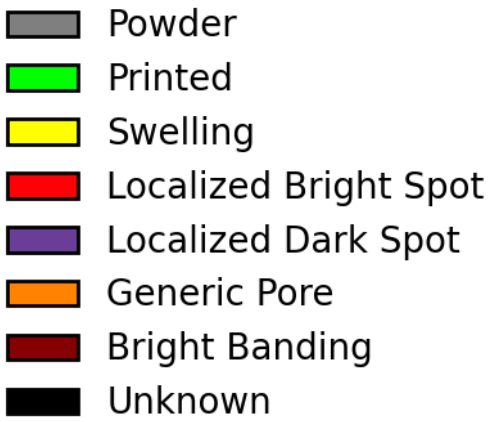

Figure 3.18. The list of anomaly classes and associated colors defined for the TPS DOE.

anomaly classes are introduced here, Generic Pore and Bright Banding. Generic Pore is a class for describing the layer immediately after engineered pores. Bright Banding is a class termed for locally brighter intensities within photodiode images. Generic Pore was trained on only 2 layers in the entire build, specifically layers after both the 100 µm and

300 µm thick pores. Layer 165 illustrating Generic Pore class is shown in Figure 3.19. Layer 165 of Bright Banding is shown in a processed photodiode image in Figure 3.20.

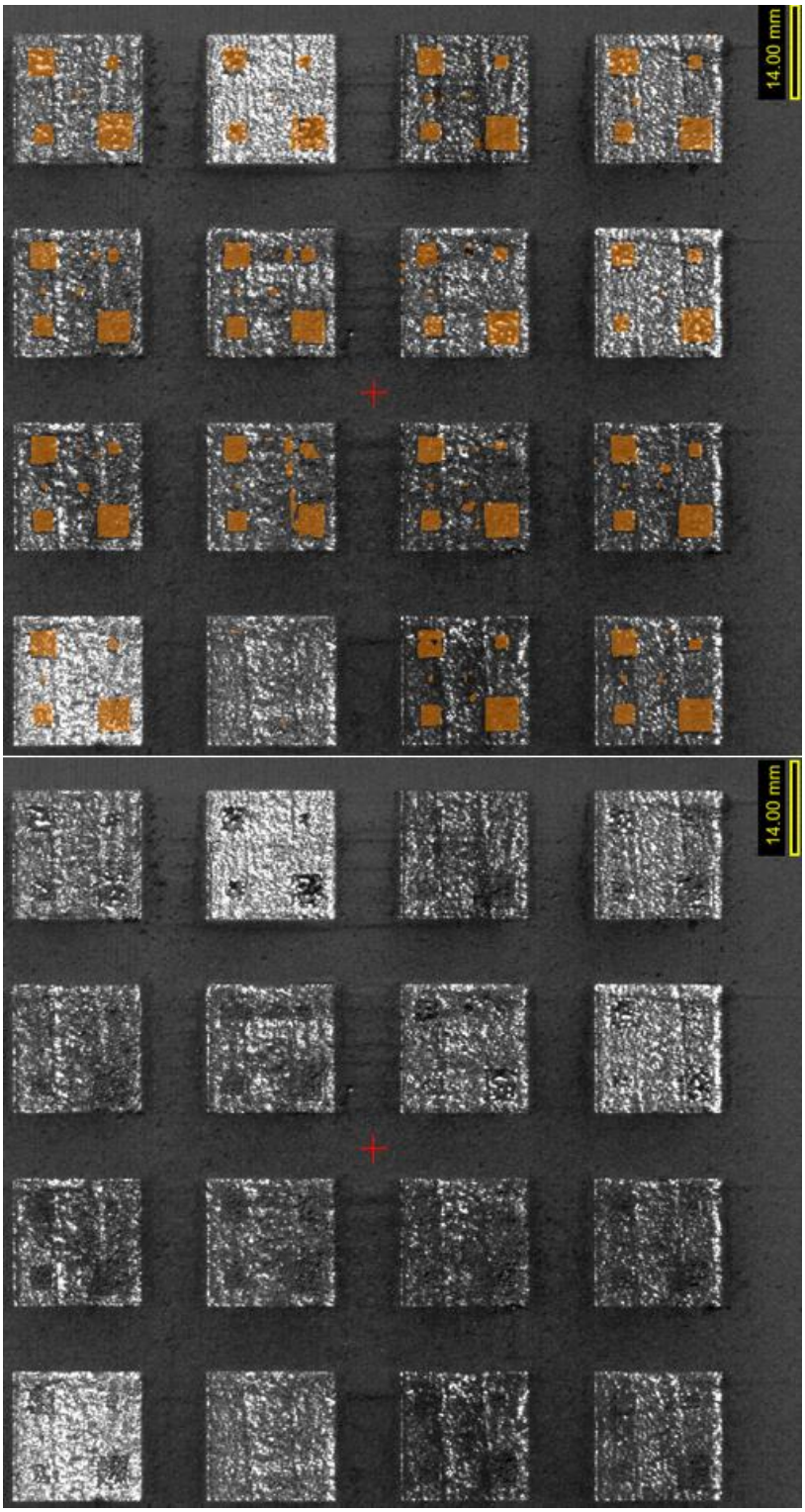

Figure 3.19. Raw post-fusion visible-light image of layer 165 (bottom) and the same image overlaid with Generic Pore classifications (top).

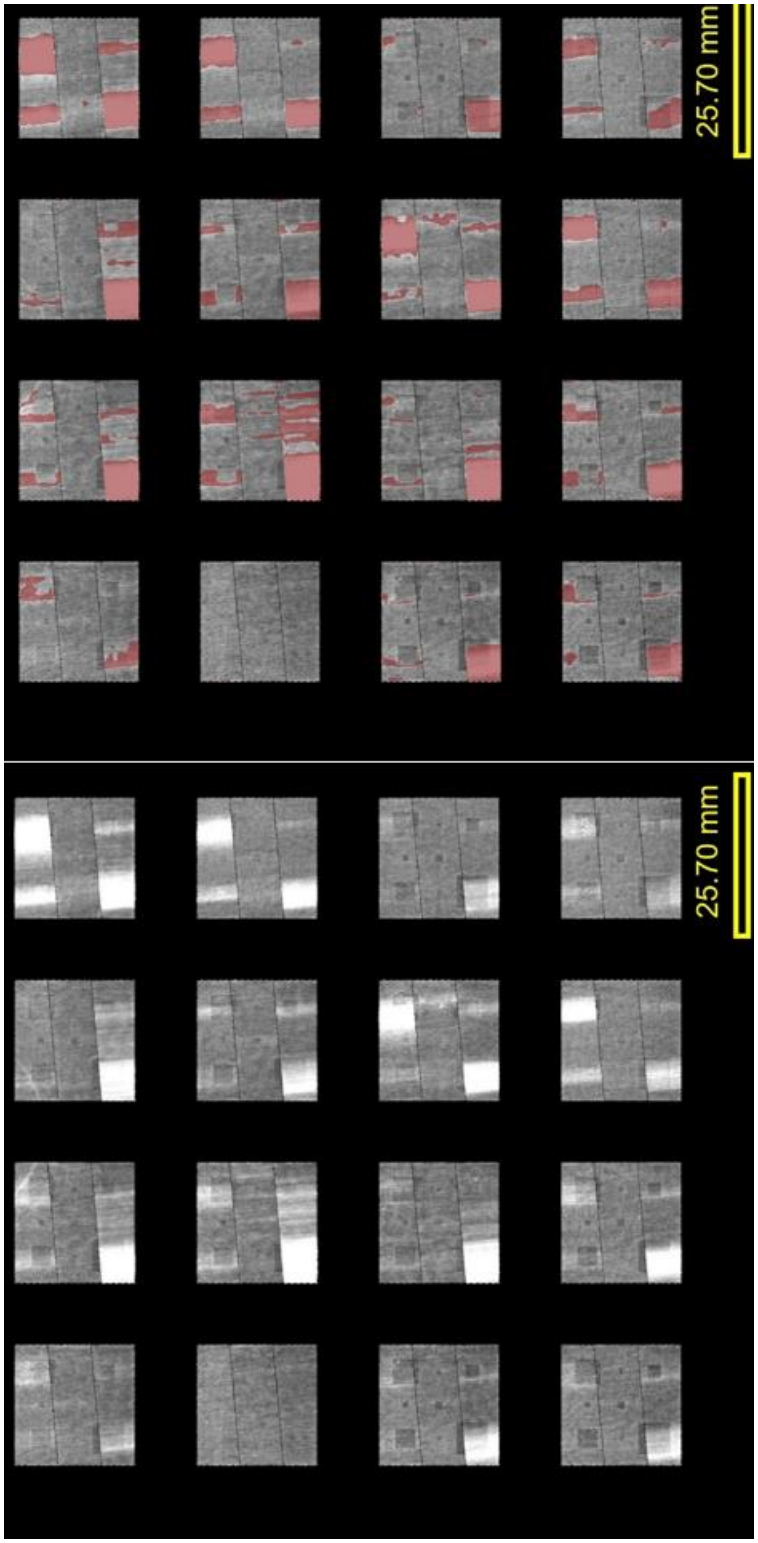

Figure 3.20. Photodiode image of TPS on layer 165 (bottom) and the same image overlaid with Bright Banding classifications (top).

Thresholding and minimum-size tools were used to train regions for this new anomaly class which typically corresponded to, but were not limited to, 5 or fewer layers immediately after engineered pores completed. Reasoning for restricting within 5 layers will be discussed in Chapter Four: *In-situ* Results section.

All cubes from the TPS DOE were removed from the plate via wire-EDM. Each part was then scanned using high resolution X-ray computed tomography (XCT) shown in Figure 3.21 using a ZEISS METROTOM 800 equipped with a 225 kV source. The system operated a peak voltage of 215 kV and an X-ray tube current of 104 µA. A total of 1013 projections were acquired for each scan at various angles and used to reconstruct a 3D representation of the scanned specimens with an 18.85 µm voxel size. Each projection was an average of 4 images with 0.5 second exposure time per acquisition.

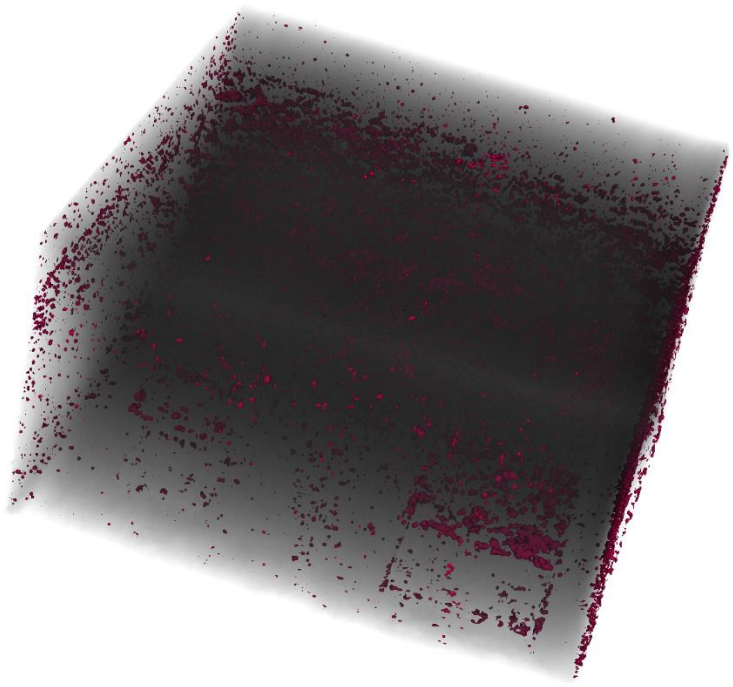

Figure 3.21, A transparent view of an arbitrary XCT volume from the TPS DOE Experiment to illustrate the presence of voids colored in red.

CHAPTER FOUR

RESULTS AND DISCUSSION

Ex-situ Results

Over 200 FT tests were performed on various 316 SS specimens. Figure 4.1 shows a breakdown of FT IR video frames before, during, and after the flash pulse occurs highlighting differences in emitted intensities on a mounted 316 SS sample. Among the first tests, this sample was prepared using a standard metallographic polishing process of 316 SS to achieve a flat face and then sand-blasted to remove reflections. The frame rate for this video was 1240 frames/second, and the pixel resolution was 250 μm/pixel.

The difference in intensities may be a result of reflectivity or absorption but are mainly attributed to a difference in local temperature. While it is difficult to decouple effects which influence temperature measurements, it does not change the fact that a thermal gradient exists. As a result, IR video frames were exported from FLIR Research Studio and parsed into MATLAB script #2 included in the Appendix. As the IR frames are stacked through time, select points may be chosen to analyze intensity vs time plots to investigate differences in intensities, decay rate parameters, or area under the curve. Figure 4.2 shows this intensity vs time plot for points of interest shown in red and green in Figure 4.1. The red point is a suspected hot spot whereas the green spot is a representative point of what is expected to be nominally dense material.

In Figure 4.2, it is observed that there is a maximum difference in temperature between the red and green points of approximately 9° Celsius throughout the transient decay of the curve. Among the initial tests, this difference seemed promising. However,

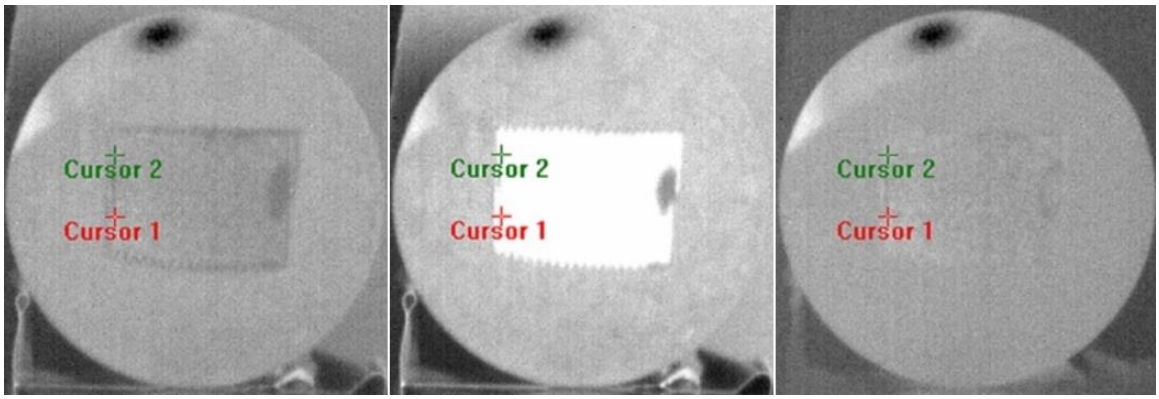

Figure 4.1. Frame by frame FT analysis of the mounted 316 SS support before flash (left) during flash (middle) and after flash (right) with two points of interest selected.

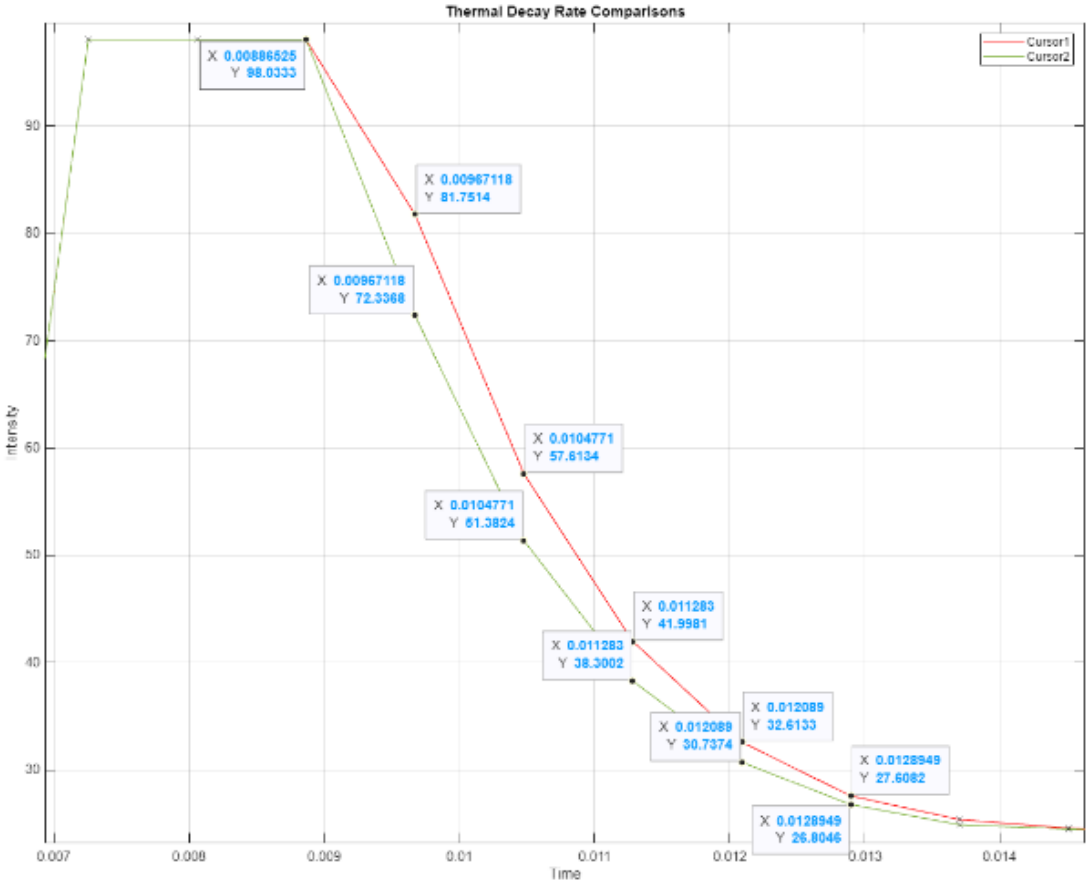

Figure 4.2. Intensity vs time plot for the red and green points shown in Figure 4.1 and a zoomed view of the transient behavior showing differences in observed temperature (right).

a surface profilometer revealed that the R_q is above 3 µm. As reported by Taylor et. al, one cannot rule out surface roughness influences on emissivity unless the ratio of emitted wavelengths to R_q is less than 0.2 [13]. Because observed wavelengths are MWIR, this ratio would be at 0.6 at best. Therefore, surface topology will generate variations in measured surface intensities and may result in false positives. Furthermore, *ex-situ* characterization techniques such as XCT would be required to test if the points of interest contained subsurface pores. Further analysis is required on a sample with known defects.

With lessons learned from initial flash tests, the two flat-bottom hole samples were tested using the method described in Chapter 3: *Ex-situ* Methods section. Figure 4.3 shows the fitted thermal decay rate parameter for each pixel across the FBH1 sample through the first 11 frames after the flash pulse. This was fit the first non-saturated frame to an exponential decay curve using MATLAB script #3 in the Appendix. 11 frames were selected to maximize the local differences observed in the thermal decay rate parameter because including 50 frames decreased contrast in local differences. However, using 11 frames after the flash pulse for the curve fit did not produce differences in the thermal decay rate parameter between the solid and subsurface pore regions, as shown in Figure 4.3. Incidentally, there are surface effects from an uneven coating of spray paint which can be seen as crescent shapes on and around flat-bottomed hole regions. These regions show greater effect on thermal decay rate parameter than regions above the FBH.

Instead of exploring thermal decay, Figure 4.4 shows the area under the curve for frames 10 -100 of the same IR video. Where Figure 4.3 may struggle to show differences in thermal decay rate across the sample, Figure 4.4 reveals locations above the high

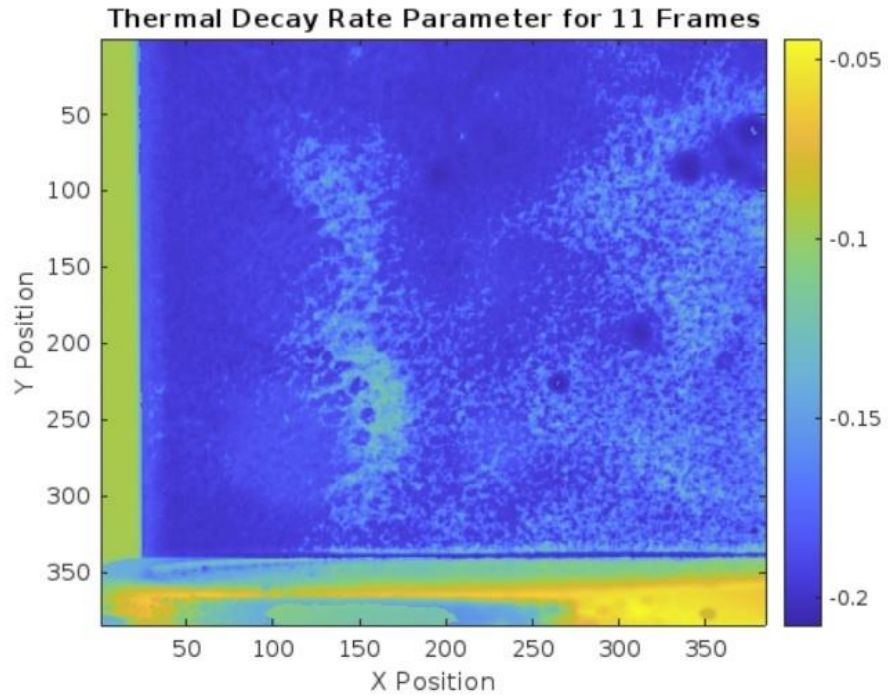

Figure 4.3. Pixelwise thermal decay parameters fitted to 11 initial frames in the transient period after flash exposure.

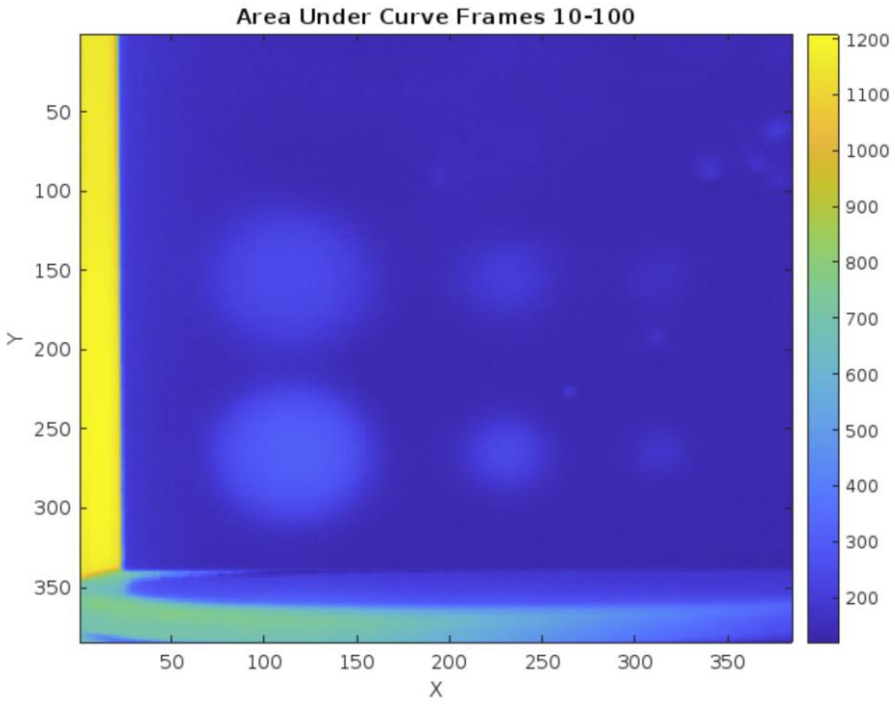

Figure 4.4. Pixelwise area under the curve emissions through time for frames excluding transient period.

aspect ratio holes. While the area under the curve of emissions through time may be influenced by factors such as processing parameter for a given application, it is a useful predictor of hole locations because the incident flash pulse is roughly uniform across the FBH surface. Therefore, the heat input into the sample is absorbed relatively instantaneously and uniformly. Because of local surface asperities, heat absorption may or may not be uniformly distributed across the FBH parts. As a result of uneven heat dispersion, the MWIR camera may observe heat radiation from just below the surface. This issue can be fixed by either surface treatment for a flatter viewing plane or by changing the irradiation pulse to a monochromatic source [59].

Figure 4.5 shows a contrast-adjusted view using histogram-equalization from a FT test of FBH1. Settings for this FT test were 536.88 frames/second with a 3kJ flash pulse. When viewing locally higher intensities like those in Figure 4.5 which correlate to the flat bottom hole features, it is easy to forget that the view shown is from the solid side of the FBH sample as shown in Figure 3.5. As heat is drawn away from the solid side, heat conduction pathways are obstructed through thickness, or Z direction, due to holes near the surface. As expected, what is revealed from Figure 4.5 are the largest and deepest flat-bottomed holes, specifically the 10 mm, 5mm, 3mm OD at 1mm and 0.750mm depth from the surface. This corresponds to hole aspect ratios ranging from 13.3 to 3.0. 1D heat transfer from Equation 1 cannot accurately represent heat transfer phenomena occurring with holes aspect ratios below aspect ratios of 3.

False positives from uneven spray coating are circled in Figure 4.6. These false positives persisted for seconds after the flash pulse and even the thermal decay of the six

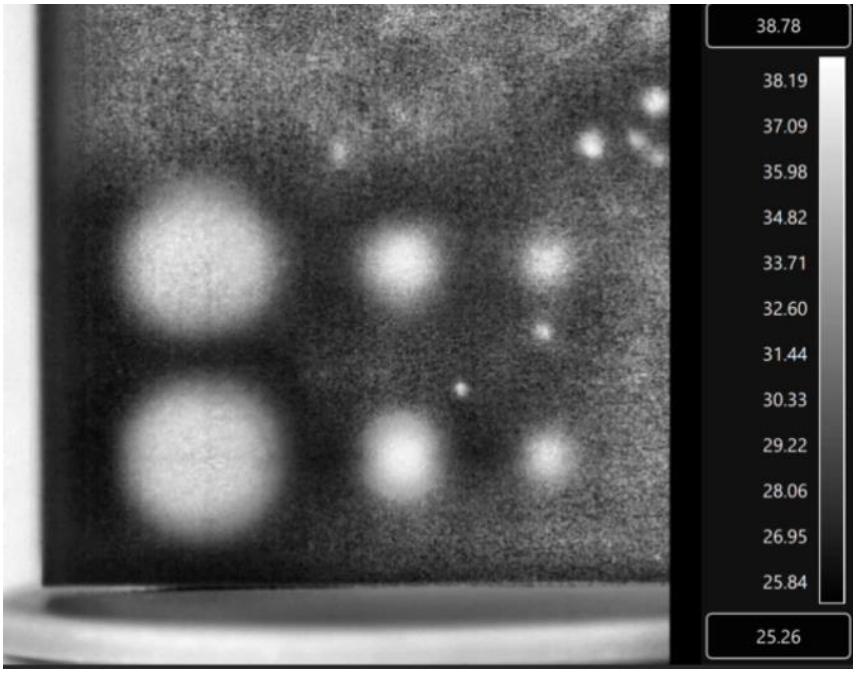

Figure 4.5. A contrast-adjusted FT frame shown after irradiation. Zones above flat-bottomed holes of ratio ≥3 emit brighter than surrounding material.

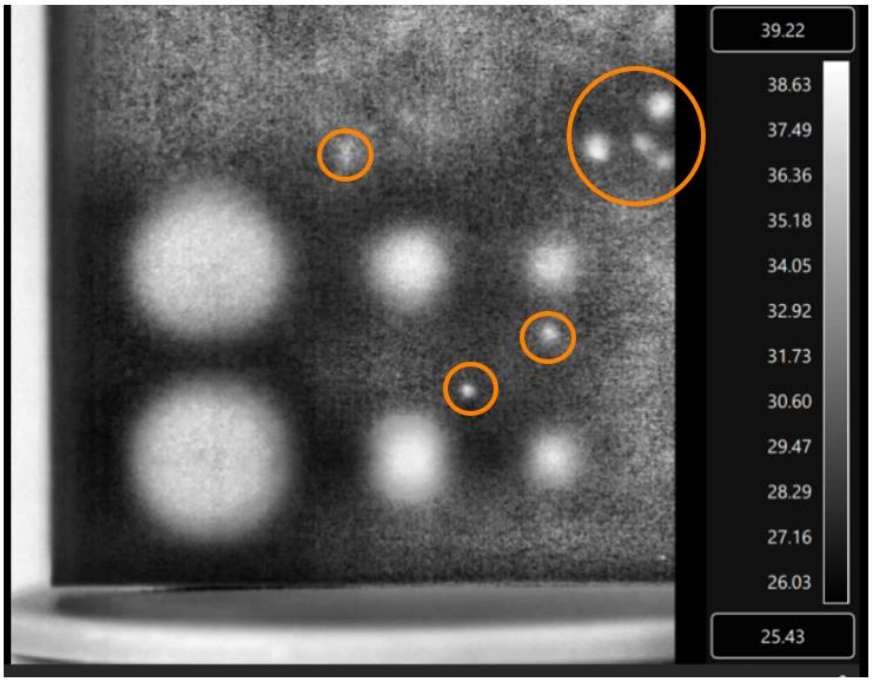

Figure 4.6. False positives from surface effects due to uneven spray-painted coating.

high aspect ratio holes. The higher emittance from the false positives can be seen in Figure 4.3 as lower thermal decay rate and Figure 4.4 as higher area under the curve.

A36 steel FBH2 specimen showed the same trends as the 316 SS FBH1 specimen in Figure 4.3 and Figure 4.4. However, with fewer frames to observe differences in thermal decay rate vs area under the curve, only the results from FBH1 are reported. This is to emphasize the utility of area under the curve as a metric as compared to thermal decay rate. Due to differences in thermal conductivities of approximately 50 W/(mK) for A36 steel vs approximately 15 W/(mK) for 316 SS, heat remains in the FBH1 longer than FBH2. Results presented here report that area under the curve is a better predictor.

Experiments have demonstrated that the *ex-situ* FT setup can test idealized components like FBH samples. However, the methodology faces challenges translating to testing of real-world components. Flat samples are required with an R_q less than 3µm. Further, surface treated with black paint is necessary to reduce the effects of emissivity and measure holes with aspect ratios > 3 to be detected reliably. In L-PBF AM, as-printed surface roughness typically exceeds 10 µm R_q on favorable planes such as XZ and YZ and 30+ µm on downskin planes such as XY. Surface treatment by spray coating or machining may not be feasible for a given part *ex-situ*. Hence, while IR-T NDE techniques are useful, the scope of FT is limited to cases with controlled surface finishes.

***In-situ* Results**

The completed TPS DOE Experiment 01 is shown in Figure 4.7 and the individual samples machined from the plate are shown in Figure 4.8. The print was

Figure 4.7. Completed TPS DOE Experiment 01 top-down view (left) and isometric view (right).

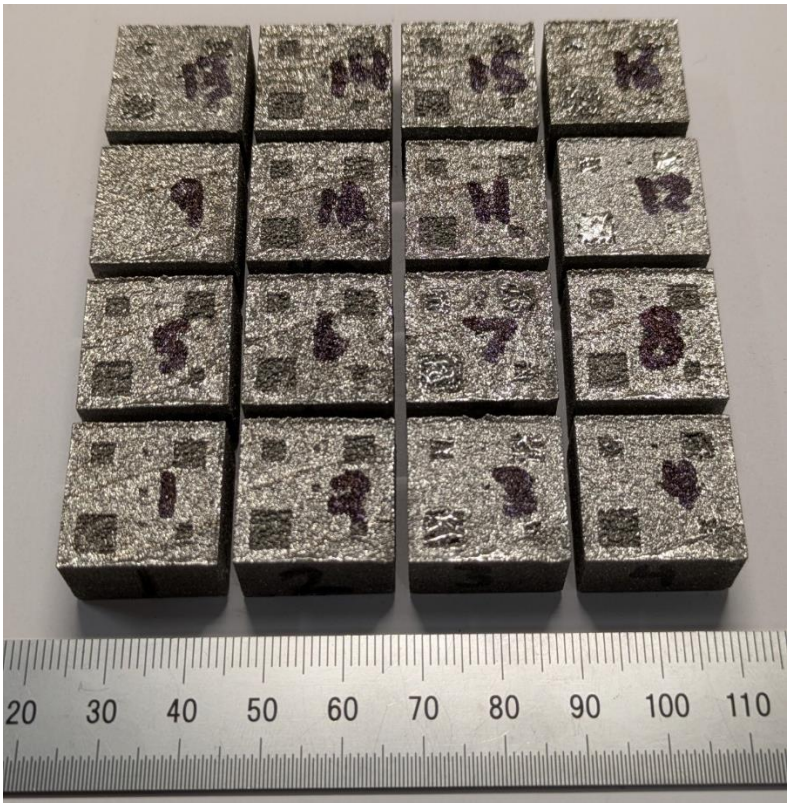

Figure 4.8. A top-down view of cubes removed from the TPS DOE build plate.

paused on the first layer after the 10-layer deep pores were melted, i.e. layer 230 or 11.5 mm of the designed 15 mm height. This allowed each part to maintain an as-printed surface, as shown in Figure 4.9, which was then measured for surface roughness.

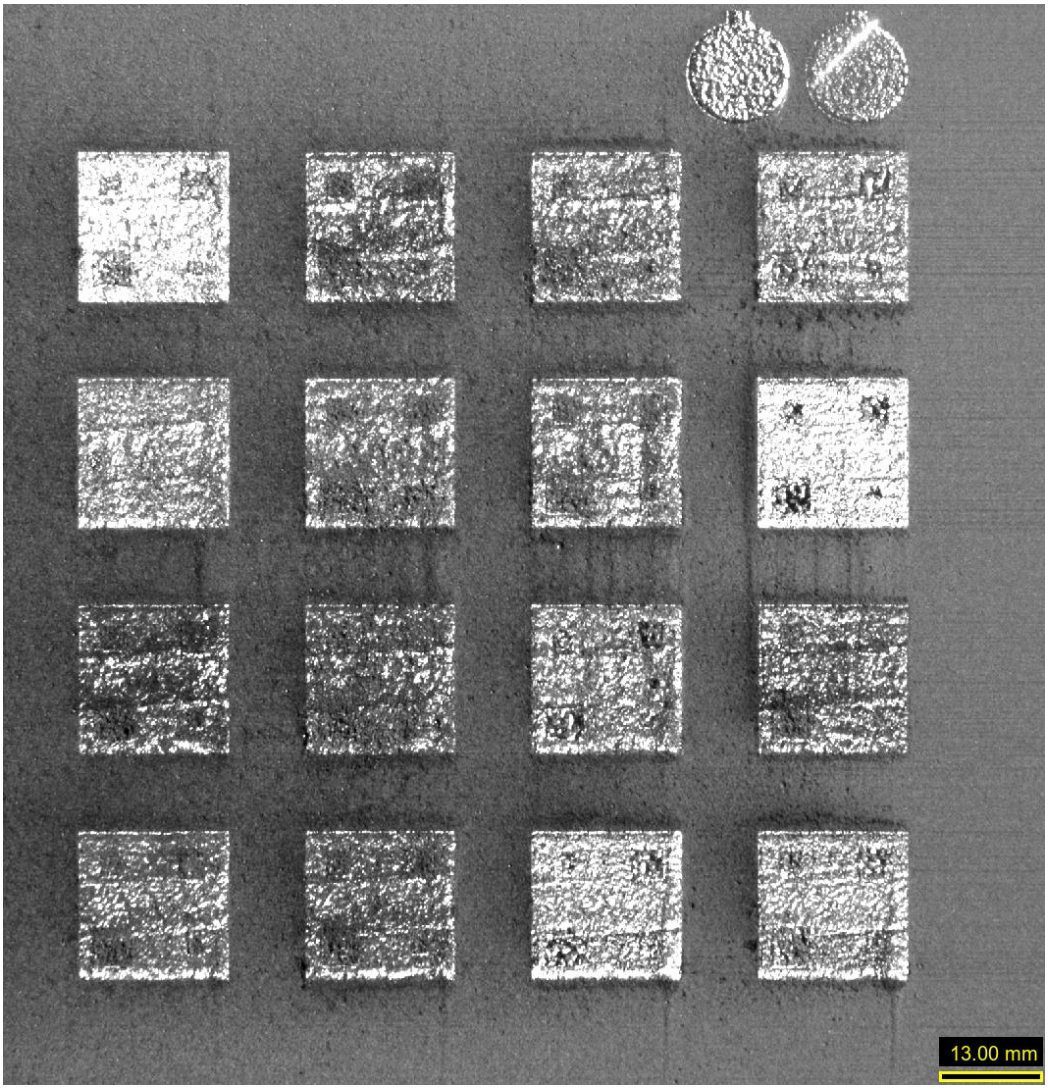

Figure 4.9. Visible-light post-fusion image of the first layer after engineered pores are completed, captured after the standard melt and TPS passes were completed.

Figure 4.10 and Figure 4.11 show the NIR thermal emissions of only the TPS pass during the experiment on a layer with engineered porosity and also the first layer after the engineered porosity 10 layers deep completed, respectively. Where exposed powder exists on a layer with engineered porosity, heat builds up from the TPS and emits brighter than surrounding solidified metal, revealed by the TPS on the right side of the left image

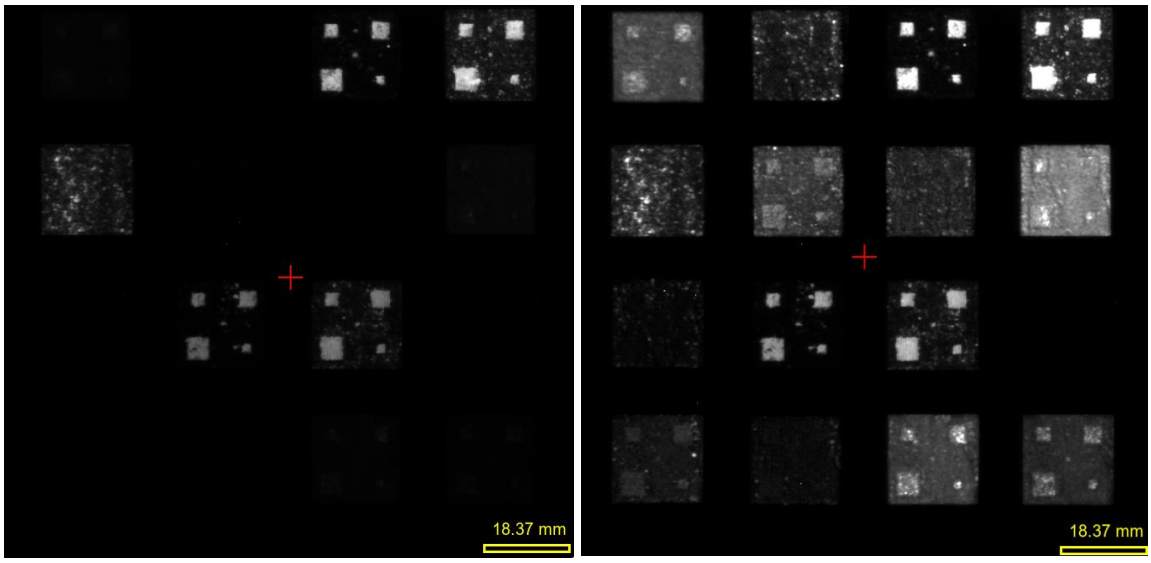

Figure 4.10. A raw grayscale NIR image of thermal emissions from only the TPS pass on a layer with engineered porosity (left) and a composite image of the same layer in which the dynamic range is adjusted for each cube (right). Note that there are no emissions from P8 as it did not include a TPS.

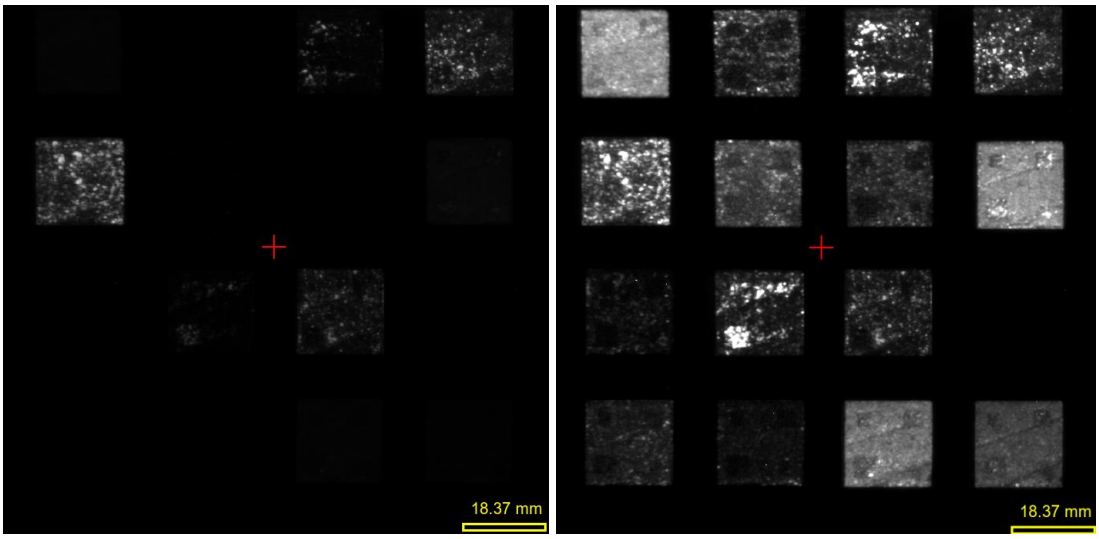

Figure 4.11. A raw grayscale NIR image of NIR thermal emissions from only the TPS on the first and only layer after the 10-layer thick engineered pores (left) and a composite image of the same layer in which the dynamic range of each cube is adjusted for each cube to highlight local intensity differences (right).

in Figure 4.10. The same trend can be seen from the photodiode intensity data shown in Figure 4.12 which shows only the melt of the layer with an engineered pore, not the TPS.

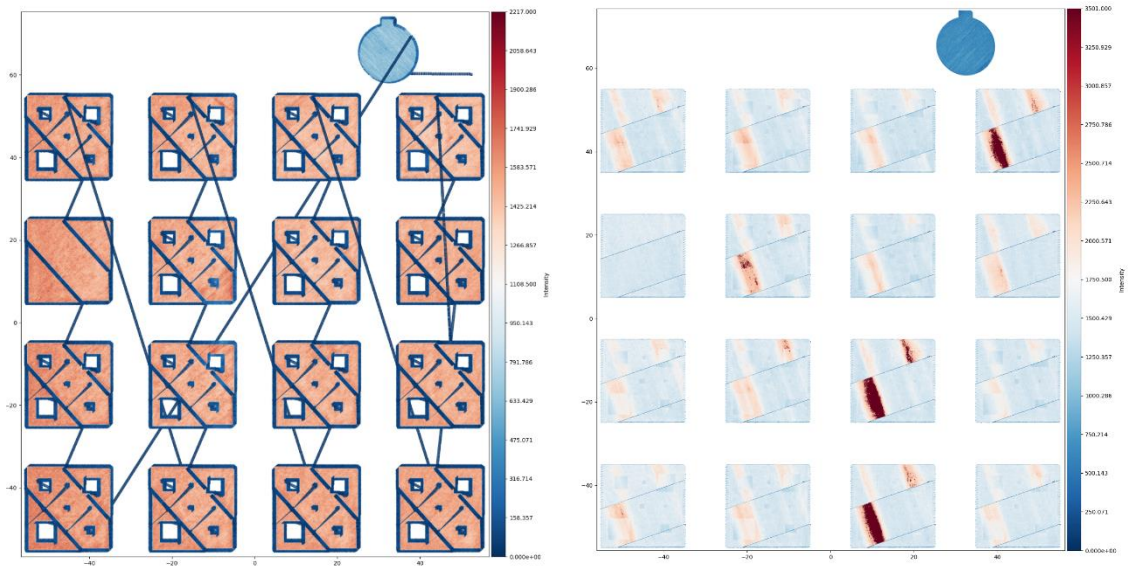

Figure 4.12. An image of photodiode intensities captured during the melt of a layer with engineered porosity (left) and an image of photodiode intensities during only the melt of all cubes melted one layer after the 10-layer engineered pore (right).

For model training, the photodiode intensities were separated by the melt and the TPS, and each dataset was then rasterized into their own images to feed into the image stack analyzed by the DMSCNN described in Figure 3.17. The photodiode data split into the melt and the TPS is shown in Figure 4.13. While the TPS parameters chosen for this experiment may have performed well to locally heat solidified metal on each layer without remelting, each was too low for the noise threshold to capture meaningful photodiode data. As a result, any analysis hereafter will consider NIR TEC data for only for the TPS and the photodiode data from only the standard melt. The completed image stack, which included three VL images, two NIR TEC images, and one photodiode image of the standard melt, were used to train the DMSCNN model as described in the *In-situ* Methods section.

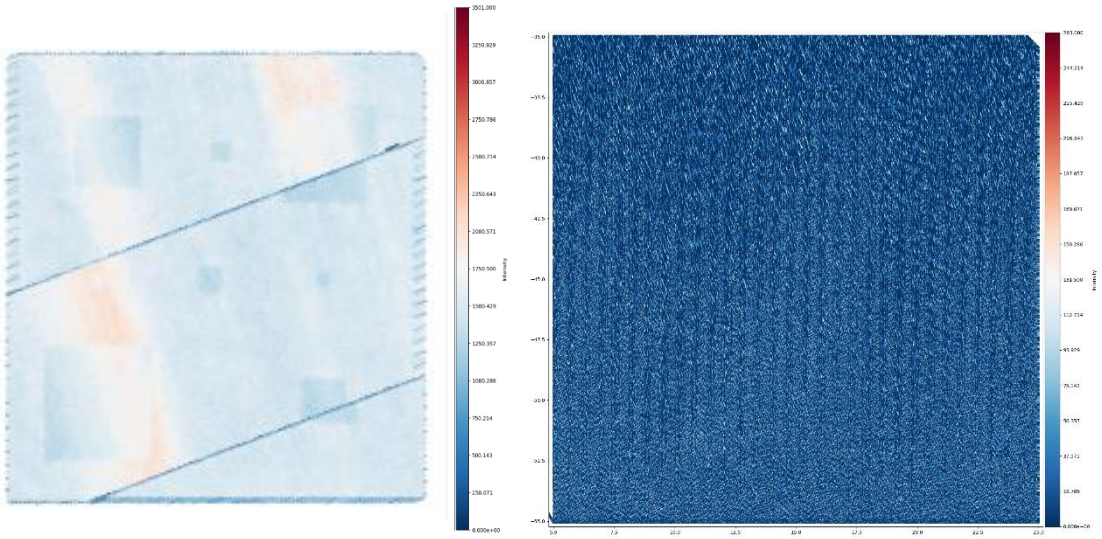

Figure 4.13. Photodiode intensity image of the standard melt for a cube one layer above the engineered porosity (left) vs aliasing effects from intensities being below the noise threshold of the photodiode sensor captured only during the TPS of the same cube (right).

Figure 4.14 shows the DMSCNN model's analysis for Layer 165 with engineered porosity. The TPS does well to reveal exposed powder by the model's ability to classify these areas as with localized bright spot (LBS) or localized dark spot (LDS). This is expected since large XY areas and deep Z volumes of either unmelted powder or trapped air or argon are more thermally insulating than the surrounding solidified metal. Therefore, data captured from the first layer which "cap" the engineered pores are most salient to this experiment's results. Note that the right side of Figure 4.10 shows TPS data on a layer with exposed powder due to engineered porosity. By and large, areas appear locally brighter than surrounding solidified metal. However, the right side of Figure 4.11 shows the first and only layer of data captured after the 10-layer deep pores completed and the trend flips such that most areas immediately above engineered pores are now locally darker than surrounding metal.

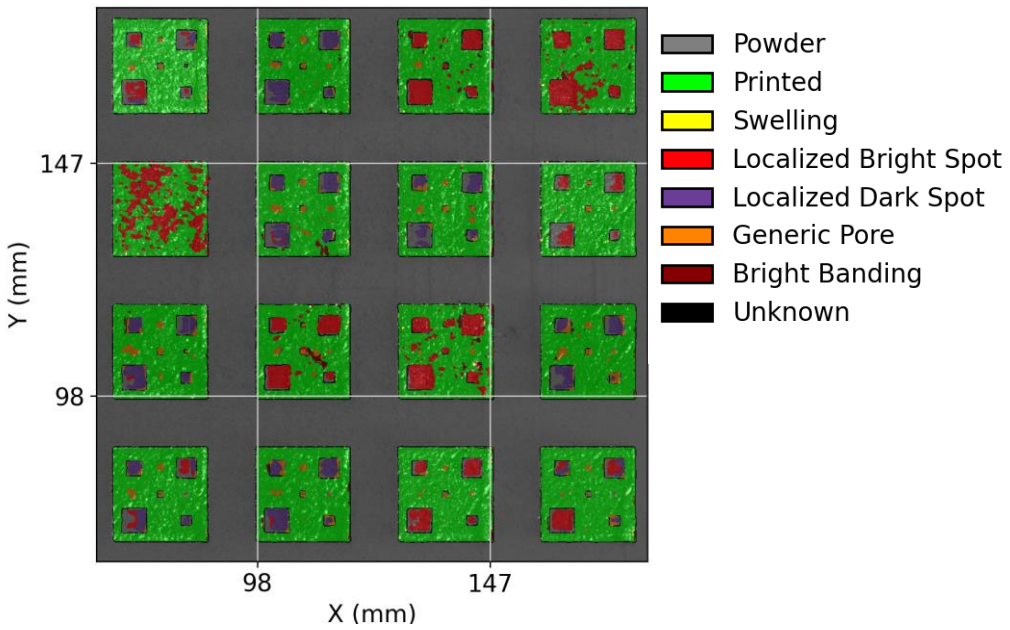

Figure 4.14. DMSCNN predictions overlayed on the post-fusion image of layer 165.

Although the root cause for this phenomenon is unknown, it is noteworthy that a certain range of TPS processing parameters is causing the observed response. This is because Parts 3, 6, 12, and 15 show brighter intensities overall or in local areas above engineered pores and were all melted with parameters whose VED was 20 J/mm³ from Table 3.2. Parameters with VED above or below 20 J/mm³ result in locally darker regions above engineered pores. Interestingly, these parameters varied spot sizes and number of passes as 50 µm vs 500 µm and single vs double passes, respectively.

Though the goal of the TPS experiment is rooted in AT, the TPS passes are not guaranteed to only thermally excite material without remelting. Given this evidence that a potentially narrow VED range results in locally higher intensities in NIR TEC images from the TPS irrespective of spot size and number of TPS passes, it is theorized that the

right amount of energy input is required to provide enough heat that will radiate back but not so much to remelt the top surface and increase thermal conductivity locally.

A Keyence VR-5000 was used to measure a height map of the top layer of the cubes shown in Figure 4.15. Recall that the experiment was intentionally stopped on the first layer completed after the designed 10-layer pores to gather surface topography data. During the experiment the author and colleagues were hopeful that locally brighter intensities would correspond to surface roughness information, specifically valleys or peaks on the surface. Qualitatively, this does not appear to be the case. There are areas in which both locally brighter intensities and locally darker intensities correspond to both higher and lower surface heights, such as parts 6 and 15 or 7 and 11, respectively. Results are inconclusive and more analysis is required to investigate this possibility.

Figure 4.12 highlights the ability of the photodiode to capture changes in melting dynamics. One complicating factor is that the photodiode is an on-axis sensor which restricts viewing the laser to build plane interaction through the laser plume. Nonetheless, high intensities are shown to persist for layers after engineered pores have completed. This is shown in Figure 4.16 and Figure 4.17 which compare photodiode intensities as a function of layers after the engineered pores as well as the depth of engineered pores. Figure 4.16**Error! Reference source not found.** highlights Part 1 for the first four layers after the 6-layer deep engineered pore was melted. Although Bright Banding appeared atop multiple pores for one layer, there are smaller streaks atop the 4 mm edge length pore in the upper right up to three layers. It is hypothesized that the scan

pattern from the standard melt, and indirectly the hatch length, is the likeliest contributor to whether Bright Banding will

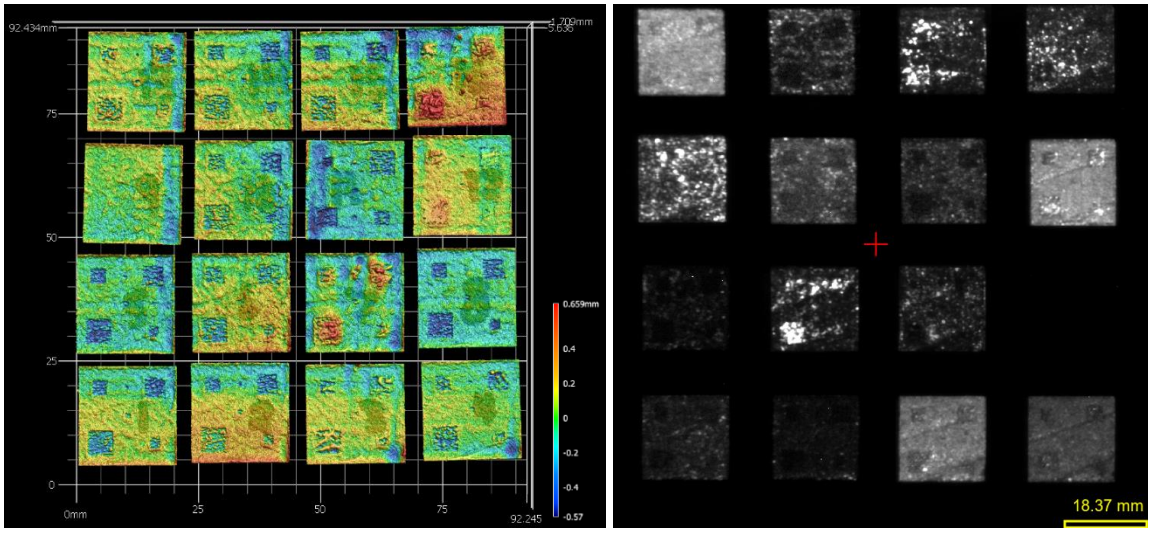

Figure 4.15. A height map captured using fringe projection (left) vs the corresponding layer's composite NIR *in-situ* image from the TPS (right).

occur multiple layers after engineered pores. Given this evidence, this is the best explanation because most other parts saw the same trend of locally higher intensities for the same 4mm and 5mm pores as shown in Figure 4.12. However, additional testing and work to explore this hypothesis is warranted to further test this theory.

Figure 4.17 also highlights part 1 and its tendency for higher and lower intensities to be detected as a function of engineered pore depth. Grayscale intensities above a given threshold were more likely to be sensed with deeper designed pores across the experiment. Although Bright Banding was introduced to describe anomalies within photodiode images irrespective of Z height, it is interesting that pores are detected as lower intensities in the photodiode data for layers after engineered pores. A confluence of factors contributes here including the processing parameter, scan strategy, emissivity

changes as a function of surface roughness, and viewing angle, contribute to specifically the LDS detected by the DMSCNN. In particular, it is posited that scan strategy and the

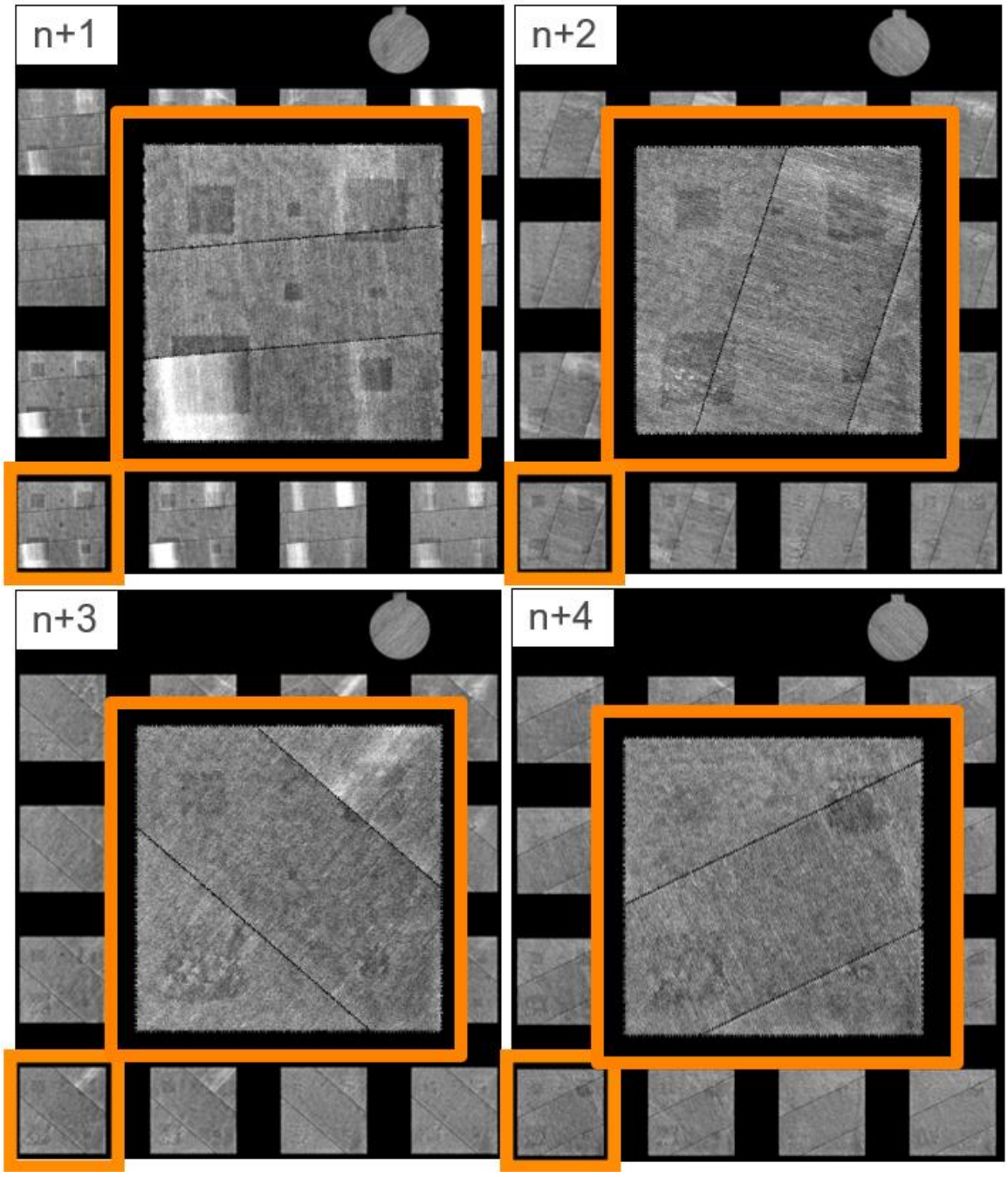

Figure 4.16. Photodiode intensity images of the melt on the first 4 layers after the 6-layer deep engineered pore. The first layer reveals simultaneously the brightest and darkest intensities classified as Bright Banding and Generic Pore, respectively.

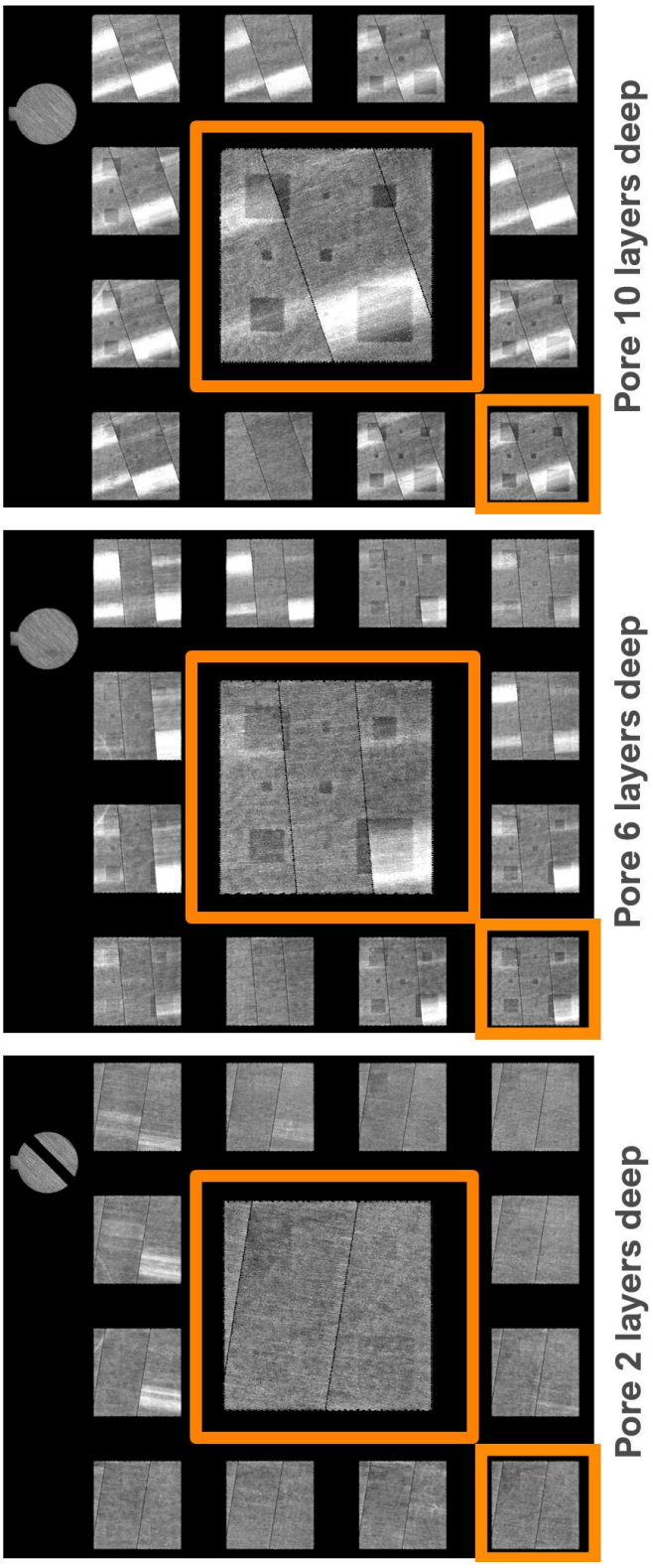

Figure 4.17. Photodiode intensity comparison of the first layer after engineered pores of varying depths.

length of vectors atop the engineered pores due to the direction of the hatch front has a strong influence on the likelihood of Bright Banding. It is possible that the shallower designed pores are healed and solidified such that higher thermal conduction paths exist through Z when observing the top surface. For engineered pores at 6- and 10-layers deep, however, healing is unlikely. The reason for detecting a lower intensity for up to four layers after closing an engineered pore as shown in Figure 4.17 is an open question and requires future research.

One major drawback of the TPS is the time added per layer. Due to relatively slow scans over large areas, the layer times for the TPS DOE Experiment increased from approximately 90 seconds minute to over 500 seconds. A 5 – 6X increase in layer times is neither desirable for L-PBF AM nor possible in many cases. Effects from an increase in layer times such as this were not investigated. Despite the added time, however, this technique does show feasibility to detect large-scale porosity down to approximately 0.5mm. Should the TPS technique be pursued, the author recommends it be restricted to critical printing areas to reduce effects from layer time increase.

Figure 4.18**Error! Reference source not found.** shows an anomaly class overlay of the last layer of the experiment highlighting the DMSCNN's reliability in classifying Bright Banding, Generic Pore, and LBS. Recall that this model is multi-class such that every pixel is classified as a yes or no for each anomaly class listed in Figure 3.18. Ultimately, the goal is to determine if these anomaly class predictions correspond to porosity detected by *ex-situ* means. In this case, XCT was used to characterize half of the

TPS DOE Experiment 01 parts. The minimum XCT intensity through the entire Z height is shown on the left of Figure 4.19

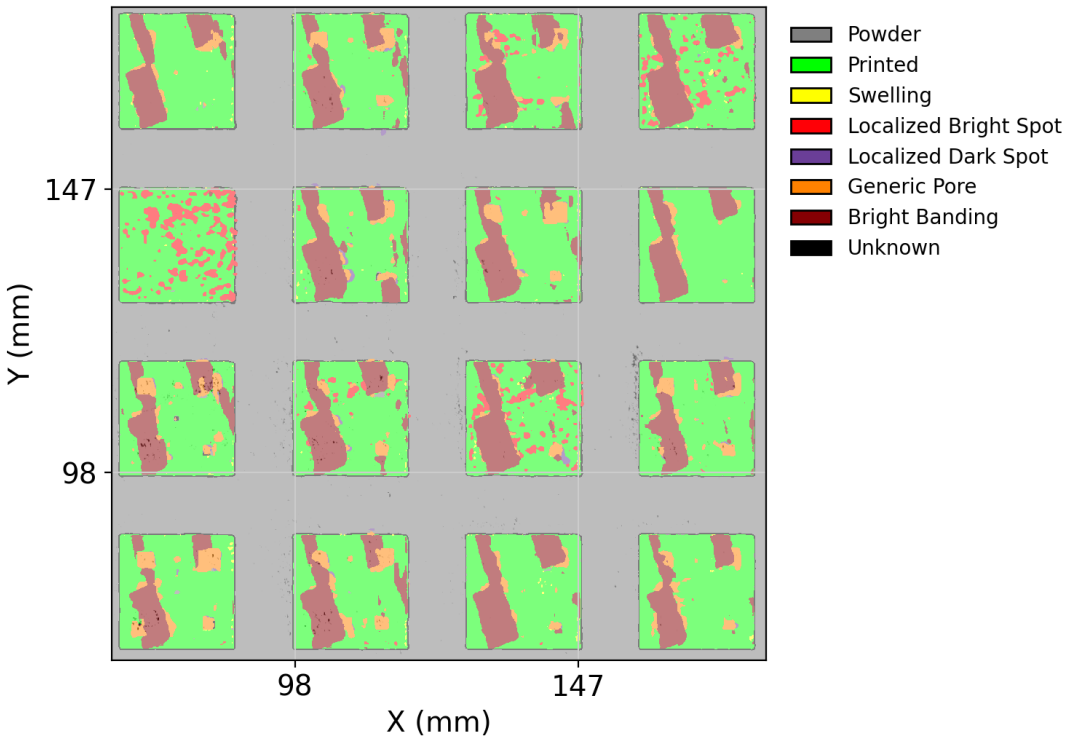

Figure 4.18. Anomaly class overlay on the VL post-fusion image of the last layer of the TPS DOE Experiment.

Figure 4.19. A composite image of the lowest intensity detected through entire Z height of the eight cubes characterized via XCT (left) and a composite image of the lowest intensity of Part 3 only through layers including the 6-layer deep engineered pore (right).

and layers through the 6-layer deep engineered pore for part 3 are shown on the right. The results from each of these datasets were then segmented into 1mm x 1mm x 0.1mm zones termed super-voxels. Using the anomaly class super-voxel results as inputs and XCT super-voxel data results as outputs, a least-squares regression model was fit. The results are shown in Table 4.1. Within each super-voxel, a number of values may be exported to classify size, morphologies, and distributions. Percent porosity was chosen as the value to measure against within each super-voxel of XCT data. The regression model fits well for a subset of P3 input data, specifically above the 6-layer engineered pore, accounting for 79.5% of spread observed in the XCT data. 11 degrees-of-freedom (DOF) were used as inputs to this model from the feature vector including all anomaly classes, some log file data, and geometric features such as distance to edge.

However, no regression model fits well to data from the part 9 control block. Although there were many classifications of LBS, Figure 4.14 and Figure 4.18 show that part 9 did not have many classifications of Generic Pore or Bright Banding as did the cubes with engineered pores. As a result, fitting a model to over 12,500 super-voxel observations using 23 inputs only accounted for 11.3% of spread seen in the XCT percent porosity data. This is likely because the mode of porosities detected in this study for the majority of super-voxel inputs was lack-of-fusion due to the size of the engineered pores. In the case of control block part 9, the manufacturer's default parameter is recommended to print parts at a minimum of 99.X% dense. This means that the default parameter for the standard melt without engineered pores is inducing less than 0.1% of porosity by means of either keyholing, boiling, or gas porosity all of which can be an order of

Table 4.1. Results from the least-squares regression fit of super-voxelized *in-situ* anomaly classifications to super-voxelized XCT porosity values.

Metric	**6-Layer Pore of P3**	**Part 9, Control**
R^2	0.795	0.113
RMS Error	4.73	3.28
Mean of Response	3.46	1.24
Observations	704	12579
Model DOF	11	23
p-values <0.001	2	8
Best input feature predictors	distance from edge, generic pore	post-spread image, distance from edge

magnitude smaller than lack-of-fusion porosity. For this reason, the TPS DOE Experiment DOE could not determine areas of porosity within the control block simply due to size. The resolution of *in-situ* image data is 86 µm for this experiment. 86 µm is, in most cases, larger than the size of porosity generated by keyholing, boiling, or gas porosity. Without overcoming hardware limitations by means of higher resolution or higher frame rate cameras, expanding thermal gradients by increasing energy input through AT, or performing more in-depth processing techniques, the methods presented in this thesis may be limited to detecting larger lack-of-fusion porosity.

CHAPTER FIVE

CONCLUSIONS AND RECOMMENDATIONS

Ex-situ Conclusions and Recommendations

Flash Thermography (FT) was performed on a range of L-PBF AM 316 stainless steel additive manufacturing (AM) parts printed by Laser-Powder Bed Fusion (L-PBF). One such part was a printed FBH specimen with holes designed with known aspect ratios. Set up in a reflection configuration, the >3 μm R_q solid side of the FBH specimen was treated with black spray paint to increase emissivity. This side of the FBH was then irradiated with a flash pulse energy of 3 – 6 kJ and subsequently observed using a FLIR 8501SC MWIR camera capturing 100 – 1000 frames per second to capture resulting surface thermal radiation. After removing saturated frames from a 7ms pulse length, the intensity vs time plots were analyzed. Thermal decay rate parameters were calculated for each pixel using 10 – 100 frames after saturated frames were removed, and total thermal emissions by area under the curve were calculated. Thermal decay rate parameters did not indicate areas immediately above hole "defects", although area under the curve showed to be a reliable predictor of hole location down to aspect ratios of 3.0.

When performing the reflection configuration FT on metal samples, the author recommends the following:

- Create a flat viewing plane to avoid surface effects on emissivity
- Treat the viewing surface with black paint to increase emissivity
- Select a viewing sensor or camera with longer wavelengths to decrease R_q to emission wavelength ratio

- Install an extender ring on the camera to maximize pixel resolution
- Maximize heat input to increase time to observe thermal decay
- Maximize number of frames to distinguish thermal transient behavior of porous and dense material
- Maximize aspect ratio of pores of interest to increase detectability

Ensuring the above points are followed will increase FT efficacy and usefulness as an *ex-situ* Non-Destructive Evaluation (NDE) technique for AM components.

In-situ Conclusions and Recommendations

Active thermography was performed in an L-PBF machine with the intent to detect subsurface porosity on layers containing engineered pores of varying sizes and depths. The test print included 16 cubes melted with the manufacturer's nominal parameter followed by a low-power laser pass termed a thermal probe scan (TPS). The experimental design varied processing parameters for the TPS to increase the *in-situ* sensors' ability to detect subsurface porosity. Before and after each melt, three images were captured using an off-axis 20MP visible-light grayscale camera. During the standard melt, one image was captured using a 40kHz near-infrared (NIR) on-axis photodiode. During the TPS, two images were captured using an off-axis low-frame rate 20MP thermal emissions camera capturing in the NIR. The layer-wise images and machine log file data were compressed for each pixel and fed into a supervised Dynamic Multiscale Convolutional Neural Network (DMSCNN) for anomaly class predictions. Experimental parts were scanned using X-Ray Computed Tomography (XCT) for porosity. Both the DMSCNN and XCT results were segmented and split into super-

voxels for localized analysis. A regression model was fit to predict percent porosity within each super-voxel using the DMSCNN's anomaly classifications as inputs and the XCT results as outputs. A subset of data from engineered pore regions achieved an R^2 value of 0.795 when fit against percent porosity. Data from the control block did not account for spread seen in the percent porosity values as its R^2 value was only 0.113.

Given the encouraging preliminary results from the regression model, future work and further analysis is recommended to explore further application. Important areas for further research and development include the following:

- Test scan strategy effects from standard melt pattern resulting in Bright Banding anomalies within photodiode image
- Increase camera resolution to increase resolving power of TPS
- Investigate effects from laser spot size including spot shape change lasers
- Explore TPS on other material systems and powder size distributions
- Utilize other sensors to increase degrees of freedom in the regression model

The TPS DOE demonstrates feasibility to detect large scale lack-of-fusion porosity *in-situ* and correlate to measured percent porosity within super-voxels. Determining ways to increase probability of detection of smaller types of porosity is key.. One particular avenue of work could be to explore the utility of raw time-resolved data from high speed on- and off-axis photodiodes to maximize the resolution of the TPS.

REFERENCES

[1] I. Gibson *et al.*, *Additive manufacturing technologies*, vol. 17. Springer, 2021.

[2] K. V. Wong and A. Hernandez, "A Review of Additive Manufacturing," *ISRN Mech. Eng.*, vol. 2012, pp. 1–10, Aug. 2012, doi: 10.5402/2012/208760.

[3] S. Singh, S. Ramakrishna, and R. Singh, "Material issues in additive manufacturing: A review," *J. Manuf. Process.*, vol. 25, pp. 185–200, Jan. 2017, doi: 10.1016/j.jmapro.2016.11.006.

[4] T. DebRoy *et al.*, "Additive manufacturing of metallic components – Process, structure and properties," *Prog. Mater. Sci.*, vol. 92, pp. 112–224, Mar. 2018, doi: 10.1016/j.pmatsci.2017.10.001.

[5] W. J. Sames, F. A. List, S. Pannala, R. R. Dehoff, and S. S. Babu, "The metallurgy and processing science of metal additive manufacturing," *Int. Mater. Rev.*, vol. 61, no. 5, pp. 315–360, Jul. 2016, doi: 10.1080/09506608.2015.1116649.

[6] Z. Snow, L. Scime, A. Ziabari, B. Fisher, and V. Paquit, "Observation of spatter-induced stochastic lack-of-fusion in laser powder bed fusion using in situ process monitoring," *Addit. Manuf.*, vol. 61, p. 103298, Jan. 2023, doi: 10.1016/j.addma.2022.103298.

[7] C. Cummings, D. J. Corbin, E. W. Reutzel, and A. R. Nassar, "Resilience of laser powder bed fusion additive manufacturing to programmatically induced laser power anomalies," *J. Laser Appl.*, vol. 35, no. 3, p. 032005, Aug. 2023, doi: 10.2351/7.0001001.

[8] F. P. Incropera, D. P. DeWitt, T. L. Bergman, and A. S. Lavine, Eds., *Principles of heat and mass transfer*, 7. ed., International student version. Hoboken, NJ: Wiley, 2013.

[9] C. Maierhofer, M. Röllig, K. Ehrig, D. Meinel, and G. Céspedes-Gonzales, "Validation of flash thermography using computed tomography for characterizing inhomogeneities and defects in CFRP structures," *Compos. Part B Eng.*, vol. 64, pp. 175–186, Aug. 2014, doi: 10.1016/j.compositesb.2014.04.027.

[10] S. C. Nagpure, R. Dinwiddie, S. S. Babu, G. Rizzoni, B. Bhushan, and T. Frech, "Thermal diffusivity study of aged Li-ion batteries using flash method," *J. Power Sources*, vol. 195, no. 3, pp. 872–876, Feb. 2010, doi: 10.1016/j.jpowsour.2009.08.025.

[11] S. Wang and N. B. Crane, "Noncontact measurement of density and thermal properties of SS 316L powder bed through flash thermography," *Rapid Prototyp. J.*, vol. 30, no. 8, pp. 1663–1674, Aug. 2024, doi: 10.1108/RPJ-01-2024-0049.

[12] J. Raplee *et al.*, "Towards process consistency and *in-situ* evaluation of porosity during laser powder bed additive manufacturing," *Sci. Technol. Weld. Join.*, vol. 25, no. 8, pp. 679–689, Nov. 2020, doi: 10.1080/13621718.2020.1823654.

[13] S. Taylor, J. B. Wright, E. C. Forrest, B. Jared, J. Koepke, and J. Beaman, "Investigating relationship between surface topography and emissivity of metallic additively manufactured parts," *Int. Commun. Heat Mass Transf.*, vol. 115, p. 104614, Jun. 2020, doi: 10.1016/j.icheatmasstransfer.2020.104614.

[14] X. P. V. Maldague, *Theory and practice of infrared technology for nondestructive testing.*, vol. 25. Portland: John Wiley & Sons, 2001.

[15] X. Maldague, F. Galmiche, and A. Ziadi, "Advances in pulsed phase thermography," *Infrared Phys. Technol.*, vol. 43, no. 3–5, pp. 175–181, Jun. 2002, doi: 10.1016/S1350-4495(02)00138-X.

[16] H. S. Carslaw and J. C. Jaeger, *Conduction of heat in solids / by H. S. Carslaw and J. C. Jaeger.*, Second edition. Oxford: Clarendon Press, 1959.

[17] V. P. Vavilov and D. D. Burleigh, "Review of pulsed thermal NDT: Physical principles, theory and data processing," *NDT E Int.*, vol. 73, pp. 28–52, Jul. 2015, doi: 10.1016/j.ndteint.2015.03.003.

[18] G. Gaussorgues, *Infrared Thermography*. Dordrecht: Springer Netherlands, 1994. doi: 10.1007/978-94-011-0711-2.

[19] G. Carlomagno and P. G. Berardi, "Unsteady thermotopography in non-destructive testing," in *Proc. 3rd Biannual Exchange, St. Louis/USA*, 1976, p. 26.

[20] W. N. Reynolds, "Thermographic methods applied to industrial materials," *Can. J. Phys.*, vol. 64, no. 9, pp. 1150–1154, Sep. 1986, doi: 10.1139/p86-200.

[21] R. Usamentiaga, P. Venegas, J. Guerediaga, L. Vega, J. Molleda, and F. Bulnes, "Infrared Thermography for Temperature Measurement and Non-Destructive Testing," *Sensors*, vol. 14, no. 7, pp. 12305–12348, Jul. 2014, doi: 10.3390/s140712305.

[22] C. Meola and G. M. Carlomagno, “Recent advances in the use of infrared thermography,” *Meas. Sci. Technol.*, vol. 15, no. 9, pp. R27–R58, Sep. 2004, doi: 10.1088/0957-0233/15/9/R01.

[23] P. Bouteille, G. Legros, H. Walaszek, and J. L. Bodnar, “Non-destructive testing of metallic materials using passive and active infrared thermography,” *Mech. Ind.*, vol. 15, no. 4, pp. 313–321, 2014, doi: 10.1051/meca/2014036.

[24] A. Foudazi, A. Mirala, M. T. Ghasr, and K. M. Donnell, “Active Microwave Thermography for Nondestructive Evaluation of Surface Cracks in Metal Structures,” *IEEE Trans. Instrum. Meas.*, vol. 68, no. 2, pp. 576–585, Feb. 2019, doi: 10.1109/TIM.2018.2843601.

[25] G. Busse, D. Wu, and W. Karpen, “Thermal wave imaging with phase sensitive modulated thermography,” *J. Appl. Phys.*, vol. 71, no. 8, pp. 3962–3965, Apr. 1992, doi: 10.1063/1.351366.

[26] D. Wu and G. Busse, “Lock-in thermography for nondestructive evaluation of materials,” *Rev. Générale Therm.*, vol. 37, no. 8, pp. 693–703, Sep. 1998, doi: 10.1016/S0035-3159(98)80047-0.

[27] W. J. Parker, R. J. Jenkins, C. P. Butler, and G. L. Abbott, “Flash Method of Determining Thermal Diffusivity, Heat Capacity, and Thermal Conductivity,” *J. Appl. Phys.*, vol. 32, no. 9, pp. 1679–1684, Sep. 1961, doi: 10.1063/1.1728417.

[28] E37 Committee, “Test Method for Thermal Diffusivity by the Flash Method,” ASTM International. doi: 10.1520/E1461-13R22.

[29] "EN 17119:2018(E) Non-destructive testing - Thermographic testing - Active thermography."

[30] S. M. Shepard, J. R. Lhota, and T. Ahmed, "Measurement limits in flash thermography," presented at the SPIE Defense, Security, and Sensing, D. D. Burleigh and R. B. Dinwiddie, Eds., Orlando, Florida, USA, May 2009, p. 72990T. doi: 10.1117/12.820062.

[31] S. M. Shepard, "Reconstruction and enhancement of active thermographic image sequences," *Opt. Eng.*, vol. 42, no. 5, p. 1337, May 2003, doi: 10.1117/1.1566969.

[32] G. Mohr *et al.*, "*In-situ* Defect Detection in Laser Powder Bed Fusion by Using Thermography and Optical Tomography—Comparison to Computed Tomography," *Metals*, vol. 10, no. 1, p. 103, Jan. 2020, doi: 10.3390/met10010103.

[33] M. A. Omar and Y. Zhou, "A quantitative review of three flash thermography processing routines," *Infrared Phys. Technol.*, vol. 51, no. 4, pp. 300–306, Mar. 2008, doi: 10.1016/j.infrared.2007.09.006.

[34] A. Heifetz *et al.*, "Thermal tomography 3D imaging of additively manufactured metallic structures," *AIP Adv.*, vol. 10, no. 10, p. 105318, Oct. 2020, doi: 10.1063/5.0016222.

[35] M. Frendberg Beemer and S. Shepard, "Aspect Ratio Considerations for Flat Bottom Hole Defects in Active Thermography," in *Proceedings of the 2016 International Conference on Quantitative InfraRed Thermography*, QIRT Council, 2016. doi: 10.21611/qirt.2016.005.

[36] J. G. Sun, “Analysis of Pulsed Thermography Methods for Defect Depth Prediction,” *J. Heat Transf.*, vol. 128, no. 4, pp. 329–338, Apr. 2006, doi: 10.1115/1.2165211.

[37] J. G. Sun, “Analysis of quantitative measurement of defects by pulsed thermal imaging,” in *AIP Conference Proceedings*, Brunswick, Maine (USA): AIP, 2002, pp. 572–576. doi: 10.1063/1.1472849.

[38] J. G. Sun, S. Erdman, and L. Connolly, “Measurement of Delamination Size and Depth in Ceramic Matrix Composites Using Pulsed Thermal Imaging,” in *Ceramic Engineering and Science Proceedings*, vol. 24, W. M. Kriven and H.-T. Lin, Eds., Hoboken, NJ, USA: John Wiley & Sons, Inc., 2003, pp. 201–206. doi: 10.1002/9780470294826.ch30.

[39] N. J. Wallace, N. B. Crane, and M. R. Jones, “Defect measurement limits using flash thermography with application to additive manufacturing,” *NDT E Int.*, vol. 128, p. 102615, Jun. 2022, doi: 10.1016/j.ndteint.2022.102615.

[40] A. Moskovchenko, M. Švantner, V. Vavilov, and A. Chulkov, “Characterizing Depth of Defects with Low Size/Depth Aspect Ratio and Low Thermal Reflection by Using Pulsed IR Thermography,” *Materials*, vol. 14, no. 8, p. 1886, Apr. 2021, doi: 10.3390/ma14081886.

[41] D. J. Chwirut, G. F. Sushinsky, D. G. Eitzen, and I. for B. Standards (U.S.), “Procedures for the calibration of ASTM E127-type ultrasonic reference blocks,” *Procedures for the calibration of ASTM E127-type ultrasonic reference blocks*. in NBS technical note ; 924. U.S. Dept. of Commerce, National Bureau of Standards,

Institute for Basic Standards : for sale by the Supt. of Docs., U.S. Govt. Print. Off., Washington, 1976.

[42] M. A. Doubenskaia, I. V. Zhirnov, V. I. Teleshevskiy, P. Bertrand, and I. Y. Smurov, “Determination of True Temperature in Selective Laser Melting of Metal Powder Using Infrared Camera,” *Mater. Sci. Forum*, vol. 834, pp. 93–102, Nov. 2015, doi: 10.4028/www.scientific.net/MSF.834.93.

[43] G. Wang, K. Yu, Y. Bai, L. Li, K. Zhang, and Y. Liu, “Melting spectral emissivity measurement of metal during the melting and solidification process,” *Energy*, vol. 300, p. 131651, Aug. 2024, doi: 10.1016/j.energy.2024.131651.

[44] D. Höfflin, C. Sauer, A. Schiffler, J. Manara, and J. Hartmann, “Pixelwise high-temperature calibration for *in-situ* temperature measuring in powder bed fusion of metal with laser beam,” *Heliyon*, vol. 10, no. 7, p. e28989, Apr. 2024, doi: 10.1016/j.heliyon.2024.e28989.

[45] G. Mohr, S. Nowakowski, S. J. Altenburg, C. Maierhofer, and K. Hilgenberg, “Experimental Determination of the Emissivity of Powder Layers and Bulk Material in Laser Powder Bed Fusion Using Infrared Thermography and Thermocouples,” *Metals*, vol. 10, no. 11, p. 1546, Nov. 2020, doi: 10.3390/met10111546.

[46] M. Y. Kayacan and N. Yılmaz, “An investigation on the measurement of instantaneous temperatures in laser assisted additive manufacturing by thermal imagers,” *Measurement*, vol. 160, p. 107825, Aug. 2020, doi: 10.1016/j.measurement.2020.107825.

[47] N. J. Wallace, “Active Thermography for Additive Manufacturing Processes”.

[48] M. Quercio *et al.*, “Application of active thermography for the study of losses in components produced by laser powder Bed fusion,” *J. Magn. Magn. Mater.*, vol. 592, p. 171796, Feb. 2024, doi: 10.1016/j.jmmm.2024.171796.

[49] D. Höfflin, C. Sauer, A. Schiffler, and J. Hartmann, “Process Monitoring Using Synchronized Path Infrared Thermography in PBF-LB/M,” *Sensors*, vol. 22, no. 16, p. 5943, Aug. 2022, doi: 10.3390/s22165943.

[50] D. Höfflin, C. Sauer, A. Schiffler, A. Versch, and J. Hartmann, “Active thermography for *in-situ* defect detection in laser powder bed fusion of metal,” *J. Manuf. Process.*, vol. 131, pp. 1758–1769, Dec. 2024, doi: 10.1016/j.jmapro.2024.09.085.

[51] P. P. Breese, T. Becker, S. Oster, C. Metz, and S. J. Altenburg, “*IN-SITU* DEFECT DETECTION FOR LASER POWDER BED FUSION WITH ACTIVE LASER THERMOGRAPHY”.

[52] F. Herzer, F. Abraham, C. Tammer, G. Schlick, C. Seidel, and J. Schilp, “Detection of Defects in Solidified Layers within Laser-based Powder Bed Fusion using Active Thermography,” *Procedia CIRP*, vol. 104, pp. 518–523, 2021, doi: 10.1016/j.procir.2021.11.087.

[53] M. Rodríguez-Martín *et al.*, “Predictive Models for the Characterization of Internal Defects in Additive Materials from Active Thermography Sequences Supported by Machine Learning Methods,” *Sensors*, vol. 20, no. 14, p. 3982, Jul. 2020, doi: 10.3390/s20143982.

[54] X. Zhang, T. Fang, J. Saniie, S. Bakhtiari, and A. Heifetz, “Unsupervised learning-enabled pulsed infrared thermographic microscopy of subsurface defects in stainless steel,” *Sci. Rep.*, vol. 14, no. 1, p. 14865, Jun. 2024, doi: 10.1038/s41598-024-64214-1.

[55] B. Stump and A. Plotkowski, “An adaptive integration scheme for heat conduction in additive manufacturing,” *Appl. Math. Model.*, vol. 75, pp. 787–805, Nov. 2019, doi: 10.1016/j.apm.2019.07.008.

[56] L. Scime and J. Beuth, “A multi-scale convolutional neural network for autonomous anomaly detection and classification in a laser powder bed fusion additive manufacturing process,” *Addit. Manuf.*, vol. 24, pp. 273–286, Dec. 2018, doi: 10.1016/j.addma.2018.09.034.

[57] L. Scime and J. Beuth, “Anomaly detection and classification in a laser powder bed additive manufacturing process using a trained computer vision algorithm,” *Addit. Manuf.*, vol. 19, pp. 114–126, Jan. 2018, doi: 10.1016/j.addma.2017.11.009.

[58] L. Scime *et al.*, “A Data-Driven Framework for Direct Local Tensile Property Prediction of Laser Powder Bed Fusion Parts,” *Materials*, vol. 16, no. 23, p. 7293, Nov. 2023, doi: 10.3390/ma16237293.

[59] S. J. Altenburg, R. Bernegger, and R. Krankenhagen, “Absorption Coefficient Dispersion in Flash Thermography of Semitransparent Solids,” *Int. J. Thermophys.*, vol. 40, no. 1, p. 13, Jan. 2019, doi: 10.1007/s10765-018-2474-0.

APPENDIX

MATLAB Script #1

```
t3 = linspace(0,5,5000);

Q = 500;   % W

pm = 8000;   % kg/m^3

pc = 3150;  % kg/m^3

pp = 1240;

cm = 500;    % 500 J/kgK

cc = 580;    % 500 J/kgK

cp = 1800;

km = 50;   % W/mK

kc = 10;  % W/mK

kp = 0.13;  % W/mK

d = 0.75e-3; % m

alpham = 15e-6; % m^2/s

alphac = 160; % m^2/s

alphap = 0.0125

Temp_metal = Q./(sqrt(pi.*pm.*cm.*km.*t3)).*exp(-d.^2./(4.*alpham.*t3));

Temp_sic = Q./(sqrt(pi.*pc.*cc.*kc.*t3)).*exp(-d.^2./(4.*alphac.*t3));

Temp_PLA = Q./(sqrt(pi.*pp.*cp.*kp.*t3)).*exp(-d.^2./(4.*alphap.*t3));

%%

Norm_Temp_metal = Temp_metal./max(Temp_PLA);

Norm_Temp_sic = Temp_sic./max(Temp_PLA);
```

```
Norm_Temp_PLA = Temp_PLA./max(Temp_PLA);
%%
% close all;
Temp_metal(1) = 0;
Temp_sic(1) = 0;
Temp_PLA(1) = 0;
Norm_Temp_metal(1) = 0;
Norm_Temp_sic(1) = 0;
Norm_Temp_PLA(1) = 0;
%%
figure
plot(t3, Norm_Temp_metal, 'k',t3, Norm_Temp_sic, 'b',t3, Norm_Temp_PLA, 'r')
xlabel('time (sec)')
ylabel('Normalized Temperature')
title('1D Heat Transfer of Different Materials')
legend('Mild steel', 'Silica', 'PLA')
xlim([-0.001,0.1])
ylim([0,1.01])
```

MATLAB Script #2

```
clear all; clc; close all;
% Chase Joslin Master's Thesis Code
% Flash Thermography Video Analyzer
```

```
% August 2024
first_frame = input("What is the first frame's index?");
last_frame = input("What is the last frame's index?");
frames = last_frame - first_frame + 1;
offset = first_frame - 1;
% Calculate the actual index in the file names
filename = sprintf('Rec-0146_73.csv');
%Read the CSV file into a matrix
video_frames = readmatrix(filename);
for index = 2:1:frames
  video_frames(:,:,index) = 0;
end
%% Read frames into 3D array
for index1 = first_frame:1:last_frame
  filename = sprintf('Rec-0146_%d.csv',index1);
  video_frames(:,:,index1-offset) = readmatrix(filename);
end
%% 2025.04.28
%% Added 2025.04.21 for Display of Individual Points Int vs time curves
% close all
row1 = 262;
col1 = 112;
```

```
row2 = 50;
col2 = 300;
frame_number = (1:1:100);
hot_spot = squeeze(video_frames(row1, col1, :));
cold_spot = squeeze(video_frames(row2, col2, :));
difference_spots = hot_spot - cold_spot;
figure
plot(frame_number', hot_spot, 'x-r', frame_number',cold_spot, 'x-g')
legend('hot spot', 'cold spot')
title('Intensity Comparison of Points')
xlabel('Frame')
ylabel('Intensity')
figure
plot(frame_number', difference_spots, 'xk-')
title('Intensity Difference')
xlabel('Frame')
ylabel('Intensity')
%% Adaptive Plateau (Histogram) Equalization 2025.04.21
Single_Frame = video_frames(:,:,12);
h = gca;
h.Visible = 'On';
figure
```

```
I = imshow(Single_Frame, [25,30])
hold on
rectangle('Position',[col1-0.5, row1-0.5, 1, 1],'EdgeColor','r','LineWidth',2)
rectangle('Position',[col2-0.5, row2-0.5, 1, 1],'EdgeColor','g','LineWidth',2)
hold off
%%
AHE_Single_Frame = histeq(Single_Frame)
figure
imshow(AHE_Single_Frame)
colorbar
%%
close all
figure
imshow(Single_Frame, [22,90])
%%
figure
imhist(Single_Frame,128)
%%
close all
figure
imshow(AHE_Single_Frame)
```

```
% adapthisteq(video_frames)
%% Display Image for User to Crop
close all;
figure
imshow(video_frames(:,:,5),[22 90])
h = gca;
h.Visible = 'On';
% At this point it is recommended the user manually crop the figure to
% determine bounds for the next step
%% Crop to region of interest
Ymin = input('Ymin');
Ymax = input('Ymax');
Xmin = input('Xmin');
Xmax = input('Xmax');
cropped_video = video_frames(Ymin:Ymax,Xmin:Xmax,1:frames);
figure
imshow(cropped_video(:,:,1),[22 25])
h = gca;
h.Visible = 'On';
%% Break for user input question
% while(1)
%    choice = menu('Press yes no','Yes','No');
```

```
%    if choice ==2 | choice==0
%      break;
%    end
% end
%% Code Hereafter is to analyze Cropped Image
% Gather initial intensity and Area under curve values
I0 = cropped_video(:,:,1);
% initialize area matrix
dimensions_cropped_video = size(cropped_video);
Area = zeros(dimensions_cropped_video(1:2));
for index1 = 1:1:dimensions_cropped_video(1)
  for index2 = 1:1:dimensions_cropped_video(2)
     Area(index1,index2) = trapz(cropped_video(index1,index2,:));
  end
end
%% Plot One Pixel's raw data Intensity vs Frame #
%close all;
% plot(test)
test = zeros(1,frames);
for index = 1:1:frames
```

```
   test(index) =
cropped_video(floor(0.5*size(cropped_video,1)),floor(0.5*size(cropped_video,2)),index)
;
end
x  = (1:1:frames)';
plot(x,test,'xk')
axis padded
hold on
% for x = 1:1:Xmax - Xmin + 1
%    for y = 1:1:Ymax - Ymin + 1
%      for z = 1:1:frames
%         test(index) = cropped_video(x,y,z);
%      end
%    end
% end
% decay_frames = input('How many decay frames do you want to include?')
decay_frames = 10;
% max(find(test == max(test)))
% fit_start = 1 + max(find(test == max(test)));
fit_start = max(find(test == max(test)));
fit_end = fit_start + decay_frames;
exponential_fit_to_test = test(fit_start:fit_end);
```

```
x_fit_start = x(fit_start:fit_end);

f = fit(x_fit_start,exponential_fit_to_test','exp1');

fit_values = coeffvalues(f);

thermal_decay_rate = fit_values(2)

%% Fourier Transform Attempt 2025.04.08

Fourier_Transform = fft(exponential_fit_to_test);

Hz = 536.88;

fs = 1/Hz;

f = (0:length(Fourier_Transform)-1)*fs/length(Fourier_Transform);

figure

plot(f,abs(Fourier_Transform))

xlabel('Frequency (Hz)')

ylabel('Magnitude')

title('Magnitude')

% plot(f,x_fit_start,exponential_fit_to_test')

% axis padded

% title('Center Point Thermay Decay')

% xlabel('Frame Number')

% ylabel('Raw Intensity')
```

MATLAB Script #3

```
%% MATLAB Script #3 assumes you have included MATLAB Script #2 to run

decay_frames = 20;
```

```
indices = size(cropped_video);
test = zeros(1,frames);
x  = (1:1:100)';
thermal_decay_rate_matrix = zeros(index1, index2);
for index1 = 1:1:indices(1)
  for index2 = 1:1:indices(2)
    for index3 = 1:1:frames
      test(index3) = cropped_video(index1,index2,index3);
    end
   % fit_start = 1 + max(find(test == max(test)));
   fit_start = max(find(test == max(test)));
   fit_end = fit_start + decay_frames;
   exponential_fit_to_test = test(fit_start:fit_end);
   x_fit_start = x(fit_start:fit_end);
   f = fit(x_fit_start,exponential_fit_to_test','exp1');
   fit_values = coeffvalues(f);
   thermal_decay_rate_matrix(index1, index2) = fit_values(2);
  end
end
%%
imagesc(thermal_decay_rate_matrix)
colorbar
```

VITA

Chase Bernard Joslin was born in East Tennessee to Cissy Poplin and Forest Joslin and graduated from the University of Tennessee, Knoxville (UTK) in 2017 with Bachelor of Science degrees in Mathematics and Materials Science and Engineering. He began working at the Manufacturing Demonstration Facility of Oak Ridge National Laboratory in 2018 under Dr. Ryan Dehoff and Dr. Michael Kirka. A metal 3D-printing experimentalist, Chase's research in Laser-Powder Bed Fusion has led or supported 30 publications, four co-registered *in-situ* to *ex-situ* datasets, two patents, and multiple industry partnerships. Returning to UTK in 2021, Chase began his Master of Science degree in Mechanical Engineering under Dr. Sudarsanam Suresh Babu and Dr. Bradley Jared. His committee included Dr. Brett Compton and Dr. Luke Scime.